

On the spin and parity of a single-produced resonance at the LHC

Sara Bolognesi,¹ Yanyan Gao,² Andrei V. Gritsan,¹ Kirill Melnikov,¹
 Markus Schulze,³ Nhan V. Tran,² and Andrew Whitbeck¹

¹*Department of Physics and Astronomy, Johns Hopkins University, Baltimore, MD, USA*

²*Fermi National Accelerator Laboratory (FNAL), Batavia, IL, USA*

³*Argonne National Laboratory (ANL), Lemont, IL, USA*

(Dated: August 20, 2012)

The experimental determination of the properties of the newly discovered boson at the Large Hadron Collider is currently the most crucial task in high energy physics. We show how information about the spin, parity, and, more generally, the tensor structure of the boson couplings can be obtained by studying angular and mass distributions of events in which the resonance decays to pairs of gauge bosons, ZZ , WW , and $\gamma\gamma$. A complete Monte Carlo simulation of the process $pp \rightarrow X \rightarrow VV \rightarrow 4f$ is performed and verified by comparing it to an analytic calculation of the decay amplitudes $X \rightarrow VV \rightarrow 4f$. Our studies account for all spin correlations and include general couplings of a spin $J = 0, 1, 2$ resonance to Standard Model particles. We also discuss how to use angular and mass distributions of the resonance decay products for optimal background rejection. It is shown that by the end of the 8 TeV run of the LHC, it might be possible to separate extreme hypotheses of the spin and parity of the new boson with a confidence level of 99% or better for a wide range of models. We briefly discuss the feasibility of testing scenarios where the resonances is not a parity eigenstate.

PACS numbers: 12.60.-i, 13.88.+e, 14.80.Bn

I. INTRODUCTION

The discovery of the new boson [1, 2] at the LHC, which is further corroborated by the strong evidence from the Tevatron [3], is the culmination of the hunt for the elusive Higgs boson. Three primary decay channels¹ $X \rightarrow ZZ$, WW , and $\gamma\gamma$ were observed experimentally by the CMS and ATLAS collaborations. However, not much is currently known about detailed properties of the new boson beyond its mass, $m_X \sim 125$ GeV, although some information can be reasoned from data. We know that the width of the new particle is consistent with being smaller than the experimental resolution of about a GeV. We also know that, as a consequence of the Landau-Yang theorem [4, 5], the new boson cannot have spin one because it decays to two on-shell photons. Finally, we know that the relative decay branching fractions and production cross-sections of the new particle are generally consistent with the Standard Model (SM) Higgs boson hypothesis [6], although current accuracy of experimental measurements does not allow for an unambiguous conclusion.

Since the new boson interacts with massive gauge bosons, we expect it to play some role in electroweak symmetry breaking. However, this needs to be verified by direct measurements of its properties. In particular, it is important to experimentally study the tensor structure of couplings of the new boson to SM fields and its $SU(2) \times U(1)$ quantum numbers (if any), avoiding theoretical prejudice. For example, we may wonder if the relatively strong interaction of the new particle with electroweak gauge bosons *already observed* implies that this new boson is not a pseudoscalar. One may argue that this is the case because a pseudoscalar must interact with gauge bosons by means of higher-dimensional operator whose significant contributions to $X \rightarrow VV$ would imply low scale physics beyond the SM (BSM) which should have already been observed experimentally. Since no BSM physics has been observed at the LHC, the scale of new physics cannot be low and it is tempting to conclude that the pseudoscalar nature of the new boson is excluded². While such arguments are appealing and may in fact be valid, it is important to test them experimentally, *especially* when such tests are within reach. In fact, as we show in this paper, it is entirely possible to achieve that with data

¹ Throughout this paper, we will use a uniform notation for both on-shell and off-shell massive gauge bosons.

² Even stronger arguments about XVV coupling by means of higher-dimensional operators are possible if one assumes that X is a singlet under electroweak $SU(2) \times U(1)$ [7].

from the 8 TeV run of the LHC using di-boson final states. Hence, it is realistic to expect that a clear profile of the new boson can be established by purely experimental means in a short period of time.

The determination of the quantum numbers of a Higgs-like particle was discussed in great detail in the literature, see Refs. [8–22]. The strategy that we use in this paper is similar to what has already been discussed in Ref. [19]. In that reference we demonstrated that X decaying to two vector bosons provides an excellent channel to study the tensor structure of its couplings and outlined the general way to do so. Since Ref. [19] was written *before* the new particle was discovered, its mass and production rates were unknown. As a result, many examples studied in Ref. [19] are, by now, of an academic interest. The discovery of the new boson allows us to extend the discussion presented in Ref. [19] and arrive at realistic predictions about the prospects for measuring its spin and couplings at the LHC.

We extend the analysis reported in Ref. [19] in several important ways. First, since the mass of the new resonance is $m_X \simeq 125$ GeV, at least one of the bosons in the $X \rightarrow ZZ/WW$ decay is off-shell. Calculations reported in Ref. [19] employed general structures of scattering amplitudes and general angular distributions but did not fully include the off-shell kinematics of the vector bosons; we improve on this in the current paper. We also extend those earlier results by including WW and $\gamma\gamma$ final states in the Monte Carlo simulation. As we stressed earlier [19], the optimal analysis for the new boson discovery and its property measurements requires utilization of the full kinematic information about the process. Analysis based on matrix elements or multivariate per-event likelihoods, such as MELA (Matrix Element Likelihood Analysis), adopted by CMS [2, 23], allows for optimal background suppression. The same techniques also guarantee the best performance when applied to measurements of the new boson’s properties.

In this paper, we consider the gluon fusion, gg , and quark-antiquark annihilation, $q\bar{q}$, production mechanisms. The primary production mode of the SM Higgs boson is expected to be gluon fusion. The inclusion of the $q\bar{q}$ production process completes all the possible initial state polarization scenarios for spin-one and spin-two resonance hypotheses thus allowing for the most general treatment of kinematics, and inclusion of all relevant spin correlations. We also note that weak Vector Boson Fusion (VBF) is expected to account for 7% to the SM Higgs boson production rate. Since jet tagging identification would reduce the experimentally observable rate even further, the contribution from the VBF topology is at the level of a few percent. As a result, we leave dedicated analysis of the VBF topology as well as the analysis of other final states in the decay of the new boson to future work.

The paper is organized as follows. In Section II we review kinematics in resonance production and decay, expanding on our earlier work in Ref. [19] and focusing on the case relevant to the observed boson mass $m_X < 2m_{Z(W)}$. In Section III we discuss the Monte-Carlo event generator for simulating production and decay of a new boson with different hypotheses for spin and tensor structure of interactions, expanding Ref. [19] to include new final states covered in this paper. In Section IV we discuss the analysis methods. We summarize the results and conclude in Section V. Detailed formulas for angular distributions and some numerical results are given in the Appendix.

II. KINEMATICS IN RESONANCE PRODUCTION AND DECAY

Before going into the discussion of how properties of the boson X can be studied, it is interesting to point out that the determination of the spin-parity of a resonance through its decays to two gauge bosons, that subsequently decay to four leptons, was first attempted more than a half-century ago, with the study of neutral pion decays $\pi^0 \rightarrow \gamma\gamma$ and $\pi^0 \rightarrow \gamma^*\gamma^* \rightarrow e^+e^-e^+e^-$. Photon polarization in $\pi^0 \rightarrow \gamma\gamma$ can be used to determine π^0 parity [5], but it is more practical to use the orientation of the planes of the Dalitz pairs in the decay $\pi^0 \rightarrow e^+e^-e^+e^-$ [24]. Further developments of these techniques were discussed in Refs. [25, 26] and additional refinements were suggested in the context of Higgs physics in Refs. [8–22] and in the context of B -physics in Refs. [27–30]. By analogy, the decay $X \rightarrow ZZ \rightarrow 4\ell$ is an excellent channel to measure the spin, parity, and tensor structure of couplings of the new boson since the full decay kinematics are experimentally accessible. In the channels $X \rightarrow WW \rightarrow 2\ell 2\nu$ and $X \rightarrow \gamma\gamma$ less kinematic information is available, but they can complement the measurements of the resonance properties. Other final states of ZZ and WW could be considered, but they typically suffer from higher backgrounds.

We begin by discussing kinematics of the process. Consider a sequence of processes

$$gg/q\bar{q} \rightarrow X(q) \rightarrow V_1(q_1)V_2(q_2), \quad V_1 \rightarrow f(q_{11})\bar{f}(q_{12}), \quad V_2 \rightarrow f(q_{21})\bar{f}(q_{22}), \quad (1)$$

that correspond to the production of a resonance X , followed by its decay to two vector bosons, followed by their decays to four fermions. The four-momenta of all particles are shown in parentheses. Momentum conservation implies $q_i = q_{i1} + q_{i2}$, $q = q_1 + q_2$. We denote the invariant mass of the i -th gauge-boson by $m_i^2 = q_i^2$ and stress that it can differ from its mass m_V^2 . We assume that the particle X is produced on the mass shell, so that $q^2 = (q_1 + q_2)^2 = m_X^2$. In what follows, we will refer to the heavier (lighter) of the two gauge bosons as V_1 (V_2), $m_1 > m_2$.

As was already described in Ref. [19], three invariant masses $m_{V_1V_2}$, m_1 , and m_2 , and six angles fully characterize the kinematics of the process in Eq. (1) in the rest frame of the resonance X . Five of these angles are illustrated in Fig. 1, while the sixth angle defines the global rotation of an event in the plane transverse to the collision axis and,

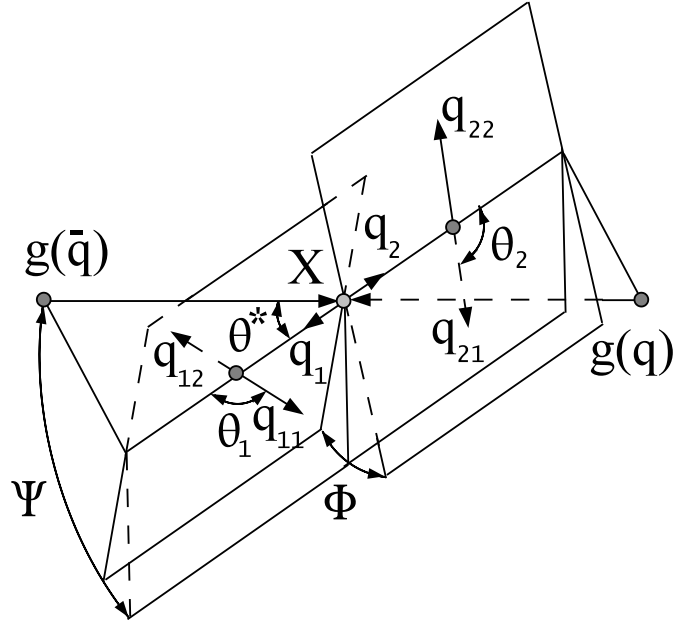


FIG. 1: Illustration of a X particle production and decay in pp collision gg or $q\bar{q} \rightarrow X \rightarrow V_1(q_1)V_2(q_2)$, $V_1 \rightarrow f(q_{11})\bar{f}(q_{12})$, $V_2 \rightarrow f(q_{21})\bar{f}(q_{22})$. The three-momenta of the fermions (f) and antifermions (\bar{f}), \mathbf{q}_{11} , \mathbf{q}_{12} , \mathbf{q}_{21} , and \mathbf{q}_{22} , are shown in their parent V_i rest-frames, and the three-momenta of the V_i bosons, \mathbf{q}_i , are shown in the X rest-frame. For sign convention of the angles between planes see text.

for this reason, it is not shown. We define these angles explicitly through the momenta of the leptons that are directly measurable experimentally.

- The angles $\theta^* \in [0, \pi]$ and $\Phi^* \in [-\pi, \pi]$ are defined through the unit vector of V_1 direction, $\hat{\mathbf{q}}_1 = (\sin \theta^* \cos \Phi^*, \sin \theta^* \sin \Phi^*, \cos \theta^*)$, in the rest frame of X . In this reference frame, the collision axis is aligned with the z -axis, $\hat{\mathbf{n}}_z = (0, 0, 1)$, taken as the direction of a colliding quark or one of the colliding gluons. Note, however, that the angle Φ^* offset is arbitrary and it is not used in the final analysis. Also, when sequential decay of the vector bosons is not available, which is the case for $X \rightarrow \gamma\gamma$, only the angle θ^* is accessible experimentally.
- The angles $\Phi \in [-\pi, \pi]$ and $\Phi_1 \in [-\pi, \pi]$ are the two azimuthal angles between the three planes constructed from the X decay products and the two V_i -boson decay products in the X rest frame. The angle $\Psi \in [-\pi, \pi]$ can be used in place of Φ_1 , it is defined as $\Psi = \Phi_1 + \Phi/2$ and can be interpreted as the angle between the parton-scattering plane and the average between the two decay planes shown in Fig. 1. These angles are explicitly defined as

$$\begin{aligned}\Phi &= \frac{\mathbf{q}_1 \cdot (\hat{\mathbf{n}}_1 \times \hat{\mathbf{n}}_2)}{|\mathbf{q}_1 \cdot (\hat{\mathbf{n}}_1 \times \hat{\mathbf{n}}_2)|} \times \cos^{-1}(-\hat{\mathbf{n}}_1 \cdot \hat{\mathbf{n}}_2), \\ \Phi_1 &= \frac{\mathbf{q}_1 \cdot (\hat{\mathbf{n}}_1 \times \hat{\mathbf{n}}_{\text{sc}})}{|\mathbf{q}_1 \cdot (\hat{\mathbf{n}}_1 \times \hat{\mathbf{n}}_{\text{sc}})|} \times \cos^{-1}(\hat{\mathbf{n}}_1 \cdot \hat{\mathbf{n}}_{\text{sc}}),\end{aligned}\quad (2)$$

where the normal vectors to the three planes are defined as

$$\hat{\mathbf{n}}_1 = \frac{\mathbf{q}_{11} \times \mathbf{q}_{12}}{|\mathbf{q}_{11} \times \mathbf{q}_{12}|}, \quad \hat{\mathbf{n}}_2 = \frac{\mathbf{q}_{21} \times \mathbf{q}_{22}}{|\mathbf{q}_{21} \times \mathbf{q}_{22}|}, \quad \text{and} \quad \hat{\mathbf{n}}_{\text{sc}} = \frac{\hat{\mathbf{n}}_z \times \mathbf{q}_1}{|\hat{\mathbf{n}}_z \times \mathbf{q}_1|}.\quad (3)$$

In the above equations, $\mathbf{q}_{i1(2)}$ is the three-momentum of a fermion (antifermion) in the decay of the V_i , and $\mathbf{q}_1 = \mathbf{q}_{11} + \mathbf{q}_{12}$ is the V_1 three-momentum, where all three-momenta are defined in the X rest frame.

- Finally, the angles θ_1 and $\theta_2 \in [0, \pi]$ are defined as

$$\theta_1 = \cos^{-1}\left(-\frac{\mathbf{q}_2 \cdot \mathbf{q}_{11}}{|\mathbf{q}_2||\mathbf{q}_{11}|}\right), \quad \theta_2 = \cos^{-1}\left(-\frac{\mathbf{q}_1 \cdot \mathbf{q}_{21}}{|\mathbf{q}_1||\mathbf{q}_{21}|}\right),\quad (4)$$

where all three-momenta are taken in the rest frame of V_i for the angle θ_i .

The invariant masses of the two-fermion final states, the six angles defined above, and four-momentum of the initial partonic state exhaust the twelve degrees of freedom available to the four particles in the final state³. The initial state four-momentum defines the X invariant mass $m_{V_1V_2}$ and the motion of the X system in the longitudinal (rapidity Y) and transverse (\mathbf{p}_T) directions. Both Y and \mathbf{p}_T distributions depend on the production mechanism and therefore could help to further differentiate production models either for signal or background. However, these observables have little discrimination power between different signal hypotheses once production and decay channels are fixed and they introduce additional systematic uncertainties due to QCD effects. It is important to point out that the transverse momentum of the X particle introduces smearing in the determination of the production angles θ^* and Ψ . The Collins-Soper frame [31] is designed to minimize the impact of the X transverse momentum on the angular measurements. However, the effect is expected to be small compared to statistical uncertainties for the luminosity expected in the 8 TeV run of the LHC and, for this reason, we do not study it in this paper.

The full differential mass and angular distribution can be expressed using Eq. (A1), where we can factorize the phase-space and propagator terms

$$\frac{d\Gamma_J(m_1, m_2, \cos\theta^*, \Psi, \cos\theta_1, \cos\theta_2, \Phi)}{dm_1 dm_2 d\cos\theta^* d\Psi d\cos\theta_1 d\cos\theta_2 d\Phi} \propto \frac{d\Gamma_J(m_1, m_2, \cos\theta^*, \Psi, \cos\theta_1, \cos\theta_2, \Phi)}{d\cos\theta^* d\Psi d\cos\theta_1 d\cos\theta_2 d\Phi} \times P(m_1, m_2), \quad (5)$$

which are defined in Ref. [13] as

$$P(m_1, m_2) = \left[1 - \frac{(m_1 + m_2)^2}{m_X^2}\right] \times \left[1 - \frac{(m_1 - m_2)^2}{m_X^2}\right] \times \frac{m_1^3}{(m_1^2 - m_V^2)^2 + m_V^2 \Gamma_V^2} \times \frac{m_2^3}{(m_2^2 - m_V^2)^2 + m_V^2 \Gamma_V^2}. \quad (6)$$

After integration over the five angles, the differential mass distribution takes the form

$$\frac{d\Gamma_J}{dm_1 dm_2} \propto \sum_{\alpha, \beta = -, 0, +} |A_{\alpha\beta}(m_1, m_2)|^2 \times P(m_1, m_2). \quad (7)$$

Below we discuss how to calculate $A_{\alpha\beta}(m_1, m_2)$ for each spin and coupling hypothesis after a brief comment on the notation that we use throughout the paper. The polarization vectors of spin-one bosons are denoted by ϵ_i ; we assume them to be transverse, $q_i \epsilon_i = 0$. Fermion wave functions are conventional Dirac spinors. The spin-two X wave function is given by a symmetric traceless tensor $t_{\mu\nu}$, transverse to its momentum $t_{\mu\nu} q^\nu = 0$; its explicit form can be found in Ref. [19]. We will often use the notation $f^{(i),\mu\nu} = \epsilon_i^\mu q_i^\nu - \epsilon_i^\nu q_i^\mu$ to denote the field strength tensor of a gauge boson with momentum q_i and polarization vector ϵ_i . Assuming that momenta of the two bosons, $V_{1,2}$, are along the z -axis $q_{1,2} = (E_{1,2}, 0, 0, \pm|\mathbf{q}|)$, the polarization vectors read

$$e_{1,2}^\mu(0) = \frac{1}{m_{1,2}} (\pm|\mathbf{q}|, 0, 0, E_{1,2}), \quad e_1^\mu(\pm) = e_2^\mu(\mp) = \frac{1}{\sqrt{2}} (0, \mp 1, -i, 0). \quad (8)$$

The conjugate field strength tensor is defined as $\tilde{f}_{\mu\nu}^{(i)} = 1/2 \epsilon_{\mu\nu\alpha\beta} f^{(i),\alpha\beta} = \epsilon_{\mu\nu\alpha\beta} \epsilon_i^\alpha q_i^\beta$. We use $\tilde{q} = q_1 - q_2$ to denote difference of momenta of the two gauge bosons.

A. Spin zero

Suppose that the new boson is a spin-zero particle. The general scattering amplitude that describes the interaction of this boson with gauge bosons reads

$$A(X \rightarrow V_1 V_2) = v^{-1} \left(g_1^{(0)} m_V^2 \epsilon_1^* \epsilon_2^* + g_2^{(0)} f_{\mu\nu}^{*(1)} f^{*(2),\mu\nu} + g_3^{(0)} f^{*(1),\mu\nu} f_{\mu\alpha}^{*(2)} \frac{q_\nu q^\alpha}{\Lambda^2} + g_4^{(0)} f_{\mu\nu}^{*(1)} \tilde{f}^{*(2),\mu\nu} \right), \quad (9)$$

where Λ denotes the scale where new physics could appear. We insert an explicit factor m_V^2 in the amplitude to allow for a smooth massless limit consistent with generic requirements of gauge invariance which is relevant in case $V = \gamma$ or g .

It is instructive to discuss the connection between the amplitude in Eq.(9) and the concept of the effective Lagrangian which is often used to discuss properties of the new boson. While the two approaches are related, the amplitude

³ Throughout the paper, we take fermions in the final state to be massless.

$A(X \rightarrow V_1 V_2)$ provides a more general description of the properties of the new boson than any effective Lagrangian because the couplings $g_i^{(0)}$ are momentum-dependent form-factors that, for example, can have both real and imaginary parts. We do not expect this issue to be important for the new boson with a mass of 125 GeV, discovered at the LHC, but it may be essential for heavier resonances that may be discovered later, so we prefer to stick to this description. On the other hand, it is also true that effective Lagrangians lead to streamlined prediction for scattering amplitudes, since they provide an opportunity to order contributions of operators of different mass dimensions by their relevance, thereby reducing the number of terms that contribute to scattering amplitudes. Of course, given the scattering amplitude and assuming that form-factors are momentum-independent constants, the corresponding Lagrangian can always be constructed. For example, in case of Eq.(9), the following correspondence is valid

$$\begin{aligned} \frac{g_1^{(0)} m_V^2}{v} \epsilon_1^* \epsilon_2^* \Leftrightarrow \mathcal{L} \sim g_1^{(0)} X Z_\mu Z^\mu, \quad \frac{g_2^{(0)}}{v} f_{\mu\nu}^{*(1)} f^{*(2),\mu\nu} \Leftrightarrow \mathcal{L} \sim \frac{g_2^{(0)}}{v} X Z_{\mu\nu} Z^{\mu\nu}, \\ g_3^{(0)} f^{*(1),\mu\nu} f_{\mu\alpha}^{*(2)} \frac{q_\nu q^\alpha}{\Lambda^2} \Leftrightarrow \mathcal{L} \sim g_3^{(0)} Z_{\mu\alpha} Z^{\nu\beta} [\partial_\beta \partial_\alpha X], \quad g_4^{(0)} f_{\mu\nu}^{*(1)} \tilde{f}^{*(2),\mu\nu} \Leftrightarrow \mathcal{L} \sim g_4^{(0)} X Z^{\mu\nu} \tilde{Z}_{\mu\nu}, \end{aligned} \quad (10)$$

where v is the vacuum expectation value of the X field. Therefore, terms with $g_1^{(0)}$ in $A(X \rightarrow V_1 V_2)$ are associated with dimension-three operators in the Lagrangian, terms with $g_2^{(0)}$ and $g_4^{(0)}$ with dimension-five, and terms with $g_3^{(0)}$ with dimension seven. As mentioned above, power-counting arguments suggest that lower-dimensional operators give larger contributions to the amplitude.

We can re-write Eq. (9) as

$$A(X \rightarrow V_1 V_2) = v^{-1} \epsilon_1^{*\mu} \epsilon_2^{*\nu} \left(a_1 g_{\mu\nu} m_H^2 + a_2 q_\mu q_\nu + a_3 \epsilon_{\mu\nu\alpha\beta} q_1^\alpha q_2^\beta \right). \quad (11)$$

The coefficients $a_{1,2,3}$ are related to $g_{1,2,3,4}^{(0)}$ by

$$a_1 = g_1^{(0)} \frac{m_V^2}{m_X^2} + \frac{s}{m_X^2} \left(2g_2^{(0)} + g_3^{(0)} \frac{s}{\Lambda^2} \right), \quad a_2 = - \left(2g_2^{(0)} + g_3^{(0)} \frac{s}{\Lambda^2} \right), \quad a_3 = -2g_4^{(0)}, \quad (12)$$

where s is defined as

$$s = q_1 q_2 = \frac{m_X^2 - m_1^2 - m_2^2}{2}. \quad (13)$$

For a spin-zero resonance with couplings shown in Eq. (11), the three contributing helicity amplitudes are

$$\begin{aligned} A_{00} &= -\frac{m_X^2}{v} \left(a_1 \sqrt{1+x} + a_2 \frac{m_1 m_2}{m_X^2} x \right), \\ A_{++} &= \frac{m_X^2}{v} \left[a_1 + i a_3 \frac{m_1 m_2}{m_X^2} \sqrt{x} \right], \\ A_{--} &= \frac{m_X^2}{v} \left[a_1 - i a_3 \frac{m_1 m_2}{m_X^2} \sqrt{x} \right], \end{aligned} \quad (14)$$

where x is defined as

$$x = \left(\frac{m_X^2 - m_1^2 - m_2^2}{2m_1 m_2} \right)^2 - 1. \quad (15)$$

For a SM Higgs boson decaying to two massive vector bosons, ZZ or WW , the values of the couplings are $g_1^{(0)} = 1$, and $g_2^{(0)} = g_3^{(0)} = g_4^{(0)} = 0$. A small value of $g_2^{(0)} \sim \mathcal{O}(\alpha_{\text{EW}}) \sim 10^{-2}$ is generated in the SM by electroweak radiative corrections. The CP -violating constant $g_4^{(0)}$ is tiny in the SM since it appears only at the three-loop level. For the SM Higgs boson decays $\gamma\gamma$, $Z\gamma$, or gg , only loop-induced couplings are possible so that $g_2^{(0)} \neq 0$ while the other couplings are zero. However, allowing for beyond the SM scenarios, values of the $g_i^{(0)}$ need to be determined experimentally. For example, for a pseudoscalar Higgs boson one would expect $g_4^{(0)} \neq 0$ while the other $g_i^{(0)} = 0$. It is also interesting to consider the model $g_2^{(0)} \neq 0$ as an alternative to the SM scalar hypothesis, or a mixture of any of the above contributions.

B. Spin one

For a spin-one resonance the amplitude depends on two independent terms

$$A(X \rightarrow V_1 V_2) = b_1 [(\epsilon_1^* q)(\epsilon_2^* \epsilon_x) + (\epsilon_2^* q)(\epsilon_1^* \epsilon_x)] + b_2 \epsilon_{\alpha\mu\nu\beta} \epsilon_x^\alpha \epsilon_1^{*\mu} \epsilon_2^{*\nu} \tilde{q}^\beta, \quad (16)$$

where ϵ_x is the polarization vector of particle X . The decay into two massless identical vector bosons is not allowed. The helicity amplitudes in the spin-one case corresponding to Eq. (16) are the following

$$\begin{aligned} A_{00} &= b_1 \frac{(m_1^2 - m_2^2)}{m_x} \sqrt{x}, \\ A_{++} &= i b_2 \frac{(m_1^2 - m_2^2)}{m_x}, \\ A_{--} &= -i b_2 \frac{(m_1^2 - m_2^2)}{m_x}, \\ A_{+0} &= b_1 m_1 \sqrt{x} + i b_2 \frac{m_2}{m_x^2} \left[\frac{1}{2} (m_x^2 - m_1^2 + m_2^2) \left(\frac{m_1^2}{m_2^2} - 1 \right) + 2m_1^2 x \right], \\ A_{0+} &= -b_1 m_2 \sqrt{x} - i b_2 \frac{m_1}{m_x^2} \left[\frac{1}{2} (m_x^2 + m_1^2 - m_2^2) \left(\frac{m_2^2}{m_1^2} - 1 \right) + 2m_2^2 x \right], \\ A_{-0} &= b_1 m_1 \sqrt{x} - i b_2 \frac{m_2}{m_x^2} \left[\frac{1}{2} (m_x^2 - m_1^2 + m_2^2) \left(\frac{m_1^2}{m_2^2} - 1 \right) + 2m_1^2 x \right], \\ A_{0-} &= -b_1 m_2 \sqrt{x} + i b_2 \frac{m_1}{m_x^2} \left[\frac{1}{2} (m_x^2 + m_1^2 - m_2^2) \left(\frac{m_2^2}{m_1^2} - 1 \right) + 2m_2^2 x \right]. \end{aligned} \quad (17)$$

The model $b_1 = g_1^{(1)} \neq 0$ corresponds to a vector particle and $b_2 = g_2^{(1)} \neq 0$ to pseudovector particle, assuming parity-conserving interactions. Even though the spin-one hypothesis is rejected by the observation of $X \rightarrow \gamma\gamma$ decay, it is still interesting to consider the spin-one models in the decay to massive vector bosons. Indeed, there could be two nearby resonances at 125 GeV, one decaying to massive gauge bosons and the other to $\gamma\gamma$, and there have been models suggested [32] which predict the presence of two resonances.

C. Spin two

For a decay of a spin-two resonance to two vector bosons, including ZZ , WW , and $\gamma\gamma$, the scattering amplitude has the following general form

$$\begin{aligned} A(X \rightarrow V_1 V_2) &= \Lambda^{-1} \left[2g_1^{(2)} t_{\mu\nu} f^{*(1)\mu\alpha} f^{*(2)\nu\alpha} + 2g_2^{(2)} t_{\mu\nu} \frac{q_\alpha q_\beta}{\Lambda^2} f^{*(1)\mu\alpha} f^{*(2)\nu\beta} + g_3^{(2)} \frac{\tilde{q}^\beta \tilde{q}^\alpha}{\Lambda^2} t_{\beta\nu} \left(f^{*(1)\mu\nu} f_{\mu\alpha}^{*(2)} + f^{*(2)\mu\nu} f_{\mu\alpha}^{*(1)} \right) \right. \\ &+ g_4^{(2)} \frac{\tilde{q}^\nu \tilde{q}^\mu}{\Lambda^2} t_{\mu\nu} f^{*(1)\alpha\beta} f_{\alpha\beta}^{*(2)} + m_V^2 \left(2g_5^{(2)} t_{\mu\nu} \epsilon_1^{*\mu} \epsilon_2^{*\nu} + 2g_6^{(2)} \frac{\tilde{q}^\mu q_\alpha}{\Lambda^2} t_{\mu\nu} (\epsilon_1^{*\nu} \epsilon_2^{*\alpha} - \epsilon_1^{*\alpha} \epsilon_2^{*\nu}) + g_7^{(2)} \frac{\tilde{q}^\mu \tilde{q}^\nu}{\Lambda^2} t_{\mu\nu} \epsilon_1^* \epsilon_2^* \right) \\ &\left. + g_8^{(2)} \frac{\tilde{q}_\mu \tilde{q}_\nu}{\Lambda^2} t_{\mu\nu} f^{*(1)\alpha\beta} \tilde{f}_{\alpha\beta}^{*(2)} + m_V^2 \left(g_9^{(2)} \frac{t_{\mu\alpha} \tilde{q}^\alpha}{\Lambda^2} \epsilon_{\mu\nu\rho\sigma} \epsilon_1^{*\nu} \epsilon_2^{*\rho} q^\sigma + \frac{g_{10}^{(2)} t_{\mu\alpha} \tilde{q}^\alpha}{\Lambda^4} \epsilon_{\mu\nu\rho\sigma} q^\rho \tilde{q}^\sigma (\epsilon_1^{*\nu} (q\epsilon_2^*) + \epsilon_2^{*\nu} (q\epsilon_1^*)) \right) \right], \end{aligned} \quad (18)$$

where $t_{\mu\nu}$ is the X wave function given by a symmetric traceless tensor [19]. This amplitude can be re-written as

$$\begin{aligned} A(X \rightarrow V_1 V_2) &= \Lambda^{-1} e_1^{*\mu} e_2^{*\nu} \left[c_1 (q_1 q_2) t_{\mu\nu} + c_2 g_{\mu\nu} t_{\alpha\beta} \tilde{q}^\alpha \tilde{q}^\beta + c_3 \frac{q_{2\mu} q_{1\nu}}{m_x^2} t_{\alpha\beta} \tilde{q}^\alpha \tilde{q}^\beta + 2c_{41} q_{1\nu} q_2^\alpha t_{\mu\alpha} + 2c_{42} q_{2\mu} q_1^\alpha t_{\nu\alpha} \right. \\ &\left. + c_5 t_{\alpha\beta} \frac{\tilde{q}^\alpha \tilde{q}^\beta}{m_x^2} \epsilon_{\mu\nu\rho\sigma} q_1^\rho q_2^\sigma + c_6 t^{\alpha\beta} \tilde{q}_\beta \epsilon_{\mu\nu\alpha\rho} q^\rho + \frac{c_7 t^{\alpha\beta} \tilde{q}_\beta}{m_x^2} (\epsilon_{\alpha\mu\rho\sigma} q^\rho \tilde{q}^\sigma q_\nu + \epsilon_{\alpha\nu\rho\sigma} q^\rho \tilde{q}^\sigma q_\mu) \right]. \end{aligned} \quad (19)$$

In case of massless bosons, like $\gamma\gamma$ or gg , the terms with m_V in Eq. (18) vanish. The coefficients c_{1-7} can be expressed through $g_{1,\dots,10}^{(2)}$

$$c_1 = 2g_1^{(2)} + 2g_2^{(2)} \frac{s}{\Lambda^2} \left(1 + \frac{m_1^2}{s} \right) \left(1 + \frac{m_2^2}{s} \right) + 2g_5^{(2)} \frac{m_V^2}{s},$$

$$\begin{aligned}
c_2 &= -\frac{g_1^{(2)}}{2} + g_3^{(2)} \frac{s}{\Lambda^2} \left(1 - \frac{m_1^2 + m_2^2}{2s}\right) + 2g_4^{(2)} \frac{s}{\Lambda^2} + g_7^{(2)} \frac{m_x^2}{\Lambda^2}, \\
c_3 &= -\left(\frac{g_2^{(2)}}{2} + g_3^{(2)} + 2g_4^{(2)}\right) \frac{m_x^2}{\Lambda^2}, \\
c_{41} &= -g_1^{(2)} - g_2^{(2)} \frac{s + m_1^2}{\Lambda^2} - g_3^{(2)} \frac{m_2^2}{\Lambda^2} - g_6^{(2)} \frac{m_V^2}{\Lambda^2}, \\
c_{42} &= -g_1^{(2)} - g_2^{(2)} \frac{s + m_2^2}{\Lambda^2} - g_3^{(2)} \frac{m_1^2}{\Lambda^2} - g_6^{(2)} \frac{m_V^2}{\Lambda^2}, \\
c_5 &= 2g_8^{(2)} \frac{m_x^2}{\Lambda^2}, \quad c_6 = g_9^{(2)} \frac{m_V^2}{\Lambda^2}, \quad c_7 = g_{10}^{(2)} \frac{m_x^2 m_V^2}{\Lambda^4}.
\end{aligned} \tag{20}$$

We note that when constructing parametrizations of parity-odd amplitudes in Eq. (18), we should carefully exploit Schouten identities to remove mutually-dependent Lorentz structures. Such dependences lead to an interesting result – it turns out that a potentially contributing term $t_{\mu\nu} f_{\alpha}^{\mu} \tilde{f}^{\nu\alpha}$ vanishes for traceless symmetric tensors, $t^{\mu\nu}$.⁴ This cancellation implies that contributions due to $t_{\mu\alpha} \tilde{q}^{\alpha} \epsilon_{\mu\nu\rho\sigma} \epsilon_1^{*\nu} \epsilon_2^{*\rho} q^{\sigma}$ and $t_{\mu\alpha} \epsilon_{1,\alpha} \epsilon_{\mu\nu\rho\sigma} \tilde{q}^{\mu} \epsilon_2^{*\rho} q^{\sigma}$ are related. Therefore, if we do not assume that the amplitude depends on $f_{\mu\nu}$ only, we could have had two Lorentz structures contributing to the amplitude. However, because the Schouten identity connects these structures, we choose to keep only one of them in Eq. (18).

We are now in a position to write down the helicity amplitudes for the spin-two case, using the parametrization shown in Eq. (19). For simplicity, we omit Λ in the following equations; the dependence on Λ can be restored on dimensional grounds. The amplitudes read

$$\begin{aligned}
A_{00} &= \frac{m_x^4}{m_1 m_2 \sqrt{6}} \frac{c_1}{8} + \frac{m_1 m_2}{\sqrt{6}} \left[c_1 \frac{1}{2} (1+x) - c_2 2x + c_{41} 2x + c_{42} 2x \right] - \frac{(m_1^4 + m_2^4) c_1}{m_1 m_2 \sqrt{6}} \frac{1}{4} + \frac{m_1 m_2 (m_1^2 - m_2^2)}{m_x^2 \sqrt{6}} (c_{41} - c_{42}) 2x \\
&+ \frac{(m_1^8 + m_2^8) c_1}{m_x^4 m_1 m_2 \sqrt{6}} \frac{1}{8} + \frac{m_1^3 m_2^3}{m_x^3 \sqrt{6}} \left[c_1 \left(\frac{3}{4} + x \right) - c_2 (4x + 8x^2) - c_3 8x^2 \right] + \frac{m_1 m_2 (m_1^4 + m_2^4)}{m_x^4 \sqrt{6}} \left[-c_1 \frac{1}{2} (1+x) + c_2 2x \right], \\
A_{++} &= \frac{m_x^2}{\sqrt{6}} \frac{c_1}{4} - \frac{(m_1^4 + m_2^4) c_1}{m_x^2 \sqrt{6}} \frac{1}{4} + \frac{m_1^2 m_2^2}{m_x^2 \sqrt{6}} \left[c_1 \left(\frac{1}{2} + x \right) + c_2 8x \right] - i \frac{m_1 m_2}{\sqrt{6}} c_6 4\sqrt{x} + i \frac{m_1^3 m_2^3}{m_x^4 \sqrt{6}} c_5 8x\sqrt{x}, \\
A_{--} &= \frac{m_x^2}{\sqrt{6}} \frac{c_1}{4} - \frac{(m_1^4 + m_2^4) c_1}{m_x^2 \sqrt{6}} \frac{1}{4} + \frac{m_1^2 m_2^2}{m_x^2 \sqrt{6}} \left[c_1 \left(\frac{1}{2} + x \right) + c_2 8x \right] - i \frac{m_1 m_2}{\sqrt{6}} c_6 4\sqrt{x} - i \frac{m_1^3 m_2^3}{m_x^4 \sqrt{6}} c_5 8x\sqrt{x}, \\
A_{+0} &= \frac{m_x^3}{m_2 \sqrt{2}} \frac{c_1}{8} + \frac{m_x m_2}{\sqrt{2}} \left(1 - \frac{m_1^2}{m_2^2} \right) \frac{c_1}{8} + \frac{m_1^2 m_2}{m_x \sqrt{2}} \left[c_1 \left(\frac{1}{4} + \frac{1}{2}x - \frac{m_2^2}{8m_1^2} - \frac{m_1^2}{8m_2^2} \right) + c_{41} 2x \right] \\
&+ \frac{m_1^2 m_2^3}{m_x^3 \sqrt{2}} c_1 \left[\frac{1}{8} \left(\frac{m_1^4}{m_2^4} - \frac{m_2^2}{m_1^2} \right) + \left(1 - \frac{m_2^2}{m_1^2} \right) \left(\frac{3}{8} + \frac{1}{2}x \right) \right] - i \frac{m_x m_1}{\sqrt{2}} c_6 \sqrt{x} + i \frac{m_1^3}{m_x \sqrt{2}} c_6 \left(1 - \frac{m_2^2}{m_1^2} \right) \sqrt{x} - i \frac{m_1^3 m_2^2}{m_x^3 \sqrt{2}} c_7 4x\sqrt{x}, \\
A_{0+} &= \frac{m_x^3}{m_1 \sqrt{2}} \frac{c_1}{8} + \frac{m_x m_1}{\sqrt{2}} \left(1 - \frac{m_2^2}{m_1^2} \right) \frac{c_1}{8} + \frac{m_1 m_2^2}{m_x \sqrt{2}} \left[c_1 \left(\frac{1}{4} + \frac{1}{2}x - \frac{m_2^2}{8m_1^2} - \frac{m_1^2}{8m_2^2} \right) + c_{42} 2x \right] \\
&+ \frac{m_1^3 m_2^2}{m_x^3 \sqrt{2}} c_1 \left[\frac{1}{8} \left(\frac{m_1^4}{m_2^4} - \frac{m_1^2}{m_2^2} \right) + \left(1 - \frac{m_2^2}{m_1^2} \right) \left(\frac{3}{8} + \frac{1}{2}x \right) \right] - i \frac{m_x m_2}{\sqrt{2}} c_6 \sqrt{x} + i \frac{m_2^3}{m_x \sqrt{2}} c_6 \left(1 - \frac{m_1^2}{m_2^2} \right) \sqrt{x} - i \frac{m_1^2 m_2^2}{m_x^3 \sqrt{2}} c_7 4x\sqrt{x}, \\
A_{-0} &= \frac{m_x^3}{m_2 \sqrt{2}} \frac{c_1}{8} + \frac{m_x m_2}{\sqrt{2}} \left(1 - \frac{m_1^2}{m_2^2} \right) \frac{c_1}{8} + \frac{m_1^2 m_2}{m_x \sqrt{2}} \left[c_1 \left(\frac{1}{4} + \frac{1}{2}x - \frac{m_2^2}{8m_1^2} - \frac{m_1^2}{8m_2^2} \right) + c_{41} 2x \right] \\
&+ \frac{m_1^2 m_2^3}{m_x^3 \sqrt{2}} c_1 \left[\frac{1}{8} \left(\frac{m_1^4}{m_2^4} - \frac{m_2^2}{m_1^2} \right) + \left(1 - \frac{m_1^2}{m_2^2} \right) \left(\frac{3}{8} + \frac{1}{2}x \right) \right] + i \frac{m_x m_1}{\sqrt{2}} c_6 \sqrt{x} - i \frac{m_1^3}{m_x \sqrt{2}} c_6 \left(1 - \frac{m_2^2}{m_1^2} \right) \sqrt{x} + i \frac{m_1^3 m_2^2}{m_x^3 \sqrt{2}} c_7 4x\sqrt{x}, \\
A_{0-} &= \frac{m_x^3}{m_1 \sqrt{2}} \frac{c_1}{8} + \frac{m_x m_1}{\sqrt{2}} \left(1 - \frac{m_2^2}{m_1^2} \right) \frac{c_1}{8} + \frac{m_1 m_2^2}{m_x \sqrt{2}} \left[c_1 \left(\frac{1}{4} + \frac{1}{2}x - \frac{m_2^2}{8m_1^2} - \frac{m_1^2}{8m_2^2} \right) + c_{42} 2x \right] \\
&+ \frac{m_1^3 m_2^2}{m_x^3 \sqrt{2}} c_1 \left[\frac{1}{8} \left(\frac{m_1^4}{m_2^4} - \frac{m_1^2}{m_2^2} \right) + \left(1 - \frac{m_2^2}{m_1^2} \right) \left(\frac{3}{8} + \frac{1}{2}x \right) \right] + i \frac{m_x m_2}{\sqrt{2}} c_6 \sqrt{x} - i \frac{m_2^3}{m_x \sqrt{2}} c_6 \left(1 - \frac{m_1^2}{m_2^2} \right) \sqrt{x} + i \frac{m_1^2 m_2^2}{m_x^3 \sqrt{2}} c_7 4x\sqrt{x},
\end{aligned}$$

⁴ We are grateful to S. Palmer and M. Baumgart for useful discussions of this point.

$$A_{+-} = A_{-+} = m_x^2 \frac{c_1}{4} + \frac{m_1^2 m_2^2}{m_x^2} c_1 x - \frac{(m_1^2 - m_2^2)^2}{m_x^2} \frac{c_1}{4}. \quad (21)$$

The minimal coupling scenario corresponds to the case $g_1^{(2)} = g_5^{(2)} \neq 0$. However, when higher-dimension operators are considered, a broader range of options becomes available, analogous to $g_2^{(0)}$ and $g_4^{(0)}$ in the spin-zero case. This variety of couplings corresponds to the complete set of vector boson V_1 and V_2 polarization states for the given m_1 and m_2 . Among non-minimal couplings, the $g_4^{(2)}$ term provides an interesting Lorentz structure with the field strength tensors of the two gauge bosons appearing similarly to the $g_2^{(0)}$ term in the spin-zero case.

We note that, in principle, all couplings that we employ in the paper should be considered functions of kinematic invariants, e.g. $g_i^{(J)}(m_x^2, q_1^2, q_2^2)$. Since the generic functional form of these couplings is unknown, accounting for dependences of $g_i^{(J)}$ on $q_{1,2}^2$ introduces additional complications that are beyond the scope of this paper. Instead, we prefer to start the spin-parity determination program by treating couplings as constants to understand the “big picture” from data. Once this is accomplished, many further refinements and, in particular, kinematic dependences of the coupling constants, can be examined. We also note that we use the same parametrization for the amplitudes that describe decays $X \rightarrow ZZ$ and $X \rightarrow W^+W^-$. In principle, since W 's are not identical particles, the number of independent form factors required to describe the most general $X \rightarrow W^+W^-$ amplitude should be larger. We neglect this effect for the reasons explained above. Similarly, we point out that for spin-one and spin-two particles, the most general parametrization of the amplitude involves terms that depend on the *difference* of invariant masses of two vector bosons so that such terms vanish on the mass shell due to Bose symmetry. We do not include such terms in the present calculation and only employ those Lorentz structures in all amplitudes that have non-vanishing on-shell limit $q_1^2 = q_2^2 = m_v^2$. While this approximation is not parametric, we believe that the current parametrization already provides sufficient variety of Lorentz structures of couplings for hypothesis testing. More sophisticated parameterizations are only warranted if credible evidence shows that non-minimal couplings that we already introduced are insufficient to describe properties of the new particle.

III. MONTE CARLO SIMULATION

We have extended the simulation program [19, 33] to allow for various di-boson final states and to include the option of resonances decaying to off-shell gauge bosons. This program simulates the production and decay to two vector bosons of the spin-zero, spin-one, and spin-two resonances in hadron-hadron collisions, including all spin correlations. The processes $gg/q\bar{q} \rightarrow X \rightarrow ZZ$ and $WW \rightarrow 4f$, as well as $gg/q\bar{q} \rightarrow X \rightarrow \gamma\gamma$, are implemented. It includes the general couplings of the X particle to gluons and quarks in production and to vector bosons in decay. The program can be interfaced to parton shower simulation (e.g. PYTHIA [34]) as well as full detector simulation through the Les Houches Event file format.

As we discussed in Sec. II, in principle there is a large number of coupling constants to be determined. To illustrate the main idea of spin-parity determination, we pick several scenarios listed in Table I. Among them we include the SM Higgs boson spin-zero hypothesis (0_m^+) and the graviton-like minimal coupling hypothesis for spin-two (2_m^+). Other, more exotic, hypotheses are also considered. We note that for the spin-two scenarios, we assume that gluon fusion

TABLE I: List of scenarios chosen for the analysis of the production and decay of an exotic X particle with quantum numbers J^P . The subscripts m (minimal couplings) and h (couplings with higher-dimension operators) distinguish different scenarios, as discussed in the last column. The spin-zero and spin-one X production parameters do not affect the angular and mass distributions, and therefore are not specified.

scenario	X production	$X \rightarrow VV$ decay	comments
0_m^+	$gg \rightarrow X$	$g_1^{(0)} \neq 0$ in Eq. (9)	SM Higgs boson scalar
0_h^+	$gg \rightarrow X$	$g_2^{(0)} \neq 0$ in Eq. (9)	scalar with higher-dimension operators
0^-	$gg \rightarrow X$	$g_4^{(0)} \neq 0$ in Eq. (9)	pseudo-scalar
1^+	$q\bar{q} \rightarrow X$	$b_2 \neq 0$ in Eq. (16)	exotic pseudo-vector
1^-	$q\bar{q} \rightarrow X$	$b_1 \neq 0$ in Eq. (16)	exotic vector
2_m^+	$g_1^{(2)} \neq 0$ in Eq. (18)	$g_1^{(2)} = g_5^{(2)} \neq 0$ in Eq. (18)	graviton-like tensor with minimal couplings
2_h^+	$g_4^{(2)} \neq 0$ in Eq. (18)	$g_4^{(2)} \neq 0$ in Eq. (18)	tensor with higher-dimension operators
2_h^-	$g_8^{(2)} \neq 0$ in Eq. (18)	$g_8^{(2)} \neq 0$ in Eq. (18)	“pseudo-tensor”

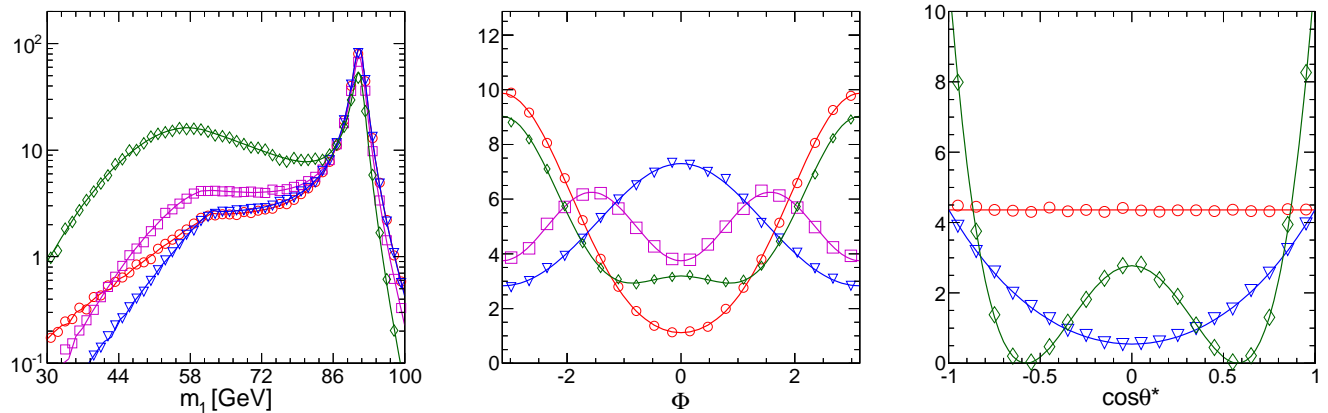


FIG. 2: Distributions of some of the representative observables: m_1 in the $X \rightarrow ZZ$ analysis (left), Φ in the $X \rightarrow WW$ analysis (middle), and $\cos\theta^*$ in the $X \rightarrow \gamma\gamma$ analysis. Four signal hypotheses are shown: SM Higgs boson (red circles), 0^- (magenta squares), 2_m^+ (blue triangles), 2_h^+ (green diamonds), as defined in Table I. Points show simulated events and lines show projections of analytical distributions. Here and throughout the paper, where only shapes of the distributions are illustrated and unless otherwise noted, units on the y axis are arbitrary.

dominates the production mechanism, which is the case for the minimal coupling Kaluza-Klein graviton (2_m^+) [17], and this assumption may have an impact on the final results for the achievable significance of spin hypotheses separation. On the other hand, for the spin-zero scenarios, the production mechanism does not affect the angular and mass distributions. The chosen scenarios listed in Table I are similar to those considered in our earlier paper [19].

Distributions of some of the representative observables are shown in Fig. 2 for $m_X = 125$ GeV. A complete set of distributions in the ZZ and WW final states is shown in Appendix B in Figs. 11, 12, 13. Throughout the paper we consider $\sqrt{s} = 8$ TeV proton-proton collisions and use the CTEQ6L1 parton distribution functions [37].

In the following we describe a simplified treatment of the detector effects which is not meant to reproduce exactly any of the LHC experiments, but still allows us to reliably understand feasibility of spin-parity studies at the LHC. We introduce smearing of the track momentum transverse to the collision axis, p_T , and photon cluster energy. However, the exact resolution parameterization is not crucial as long as the overall signal-to-background separation is reproduced well. We mimic detector acceptance effects by cutting on geometric and kinematic parameters, such as p_T and pseudorapidity, $\eta = -\ln \tan(\theta/2)$. Both leptons and photons are required to be in the effective acceptance range $|\eta| < 2.5$.

The main backgrounds in the $X \rightarrow ZZ$, WW , and $\gamma\gamma$ analyses are the continuum di-boson production, including $Z\gamma^*$ for ZZ [1, 2]. These are modeled with POWHEG [35] (ZZ) and MadGraph [36] ($WW, \gamma\gamma$). Additional contributions of backgrounds with fake vector boson reconstruction requires special treatment. However, their contributions are smaller and observable distributions are similar to the VV background, so their contributions can be effectively accounted for by rescaling the di-boson background rate to match total background rates observed by the LHC experiments.

IV. ANALYSIS METHODS

In this Section, we illustrate the application of the matrix element analysis formalism to distinguishing different spin-parity hypotheses for the observed boson near 125 GeV. We illustrate this with the seven scenarios defined in Table I and comment on future direction of the measurements.

In Ref. [19] we pointed out that the ultimate goal of the analysis should be the experimental determination of all helicity amplitudes that involve X and two gauge bosons. The techniques discussed here and in Ref. [19] are ideally suited for such measurements since parameters in the angular and mass distributions become fit parameters in analysis of data. However, such multi-parameter fits require large samples of the signal events which are not yet available. Therefore, in our opinion, the first step in understanding the spin-parity of the resonance should be distinguishing between different hypotheses. For such a goal, a simplified, but still optimal, analysis approach can be developed that employs just two observables. A simple extension of this analysis, which naturally arises if we assume, for example, that the observed resonance is a mixed spin-parity state, is to fit for ratios of couplings. Ultimately, this approach will lead to a complete multi-dimensional fit of all coupling parameters using a complete set of kinematic observables.

TABLE II: Expected separation significance (Gaussian σ) between the SM Higgs boson scenario (0_m^+) and various J_x^P hypotheses defined in Table I. Expectations are given for the scenario of a 5.0σ signal-to-background separation observed in the search for the SM Higgs boson in each channel, and therefore interpretation in terms of integrated luminosity and pp collision energy at the LHC may differ significantly between the three channels $X \rightarrow ZZ$, WW , and $\gamma\gamma$.

scenario	$X \rightarrow ZZ$	$X \rightarrow WW$	$X \rightarrow \gamma\gamma$
0_m^+ vs background	5.0	5.0	5.0
0_m^+ vs 0_h^+	1.8	1.1	0.0
0_m^+ vs 0^-	2.9	1.2	0.0
0_m^+ vs 1^+	2.1	2.0	–
0_m^+ vs 1^-	2.8	3.2	–
0_m^+ vs 2_m^+	1.1	2.8	2.4
0_m^+ vs 2_h^+	~ 5	1.1	3.1
0_m^+ vs 2_h^-	~ 5	2.5	3.1

Going back to the two-dimensional fit, we note that one of the two observables is related to the resonance mass as it typically has the largest discriminating power against the background. This observable depends on the final state; for example, it is the four-lepton invariant mass $m_{4\ell}$ in the $X \rightarrow ZZ \rightarrow 4\ell$ analysis, the transverse mass m_T [1, 2] in the $X \rightarrow WW \rightarrow 2\ell 2\nu$ analysis, or the two-photon invariant mass $m_{\gamma\gamma}$ in the $X \rightarrow \gamma\gamma$ analysis.

The second observable combines other kinematic information that is available, and it is designed to distinguish between different signal spin-parity hypotheses in the optimal way. In the $X \rightarrow ZZ \rightarrow 4\ell$ analysis we build the kinematic discriminant, defined in the MELA approach adopted by the CMS experiment [2, 23], which combines the five angular and two mass observables in the optimal way. In the $X \rightarrow WW \rightarrow 2\ell 2\nu$ analysis, the complete matrix element information cannot be exploited because of the neutrinos in the final state. Therefore, we adopt a simplified approach by picking one observable that is most sensitive to the spin-parity of X . We found this observable to be the di-lepton invariant mass $m_{\ell\ell}$ while the opening angle between the two leptons in the transverse plane provides less sensitivity. Finally, in the $X \rightarrow \gamma\gamma$ analysis, the only available observable is $\cos\theta^*$ since there is no further sequential decay chain involved.

We note that it is not our goal in this paper to demonstrate how the analysis should be optimized for the signal-background separation. Doing so requires simulation of detector performance and of all background processes [1, 2]. Instead, we assume an excess of signal events over background in each of the three channels, $X \rightarrow ZZ$, WW , and $\gamma\gamma$, and calculate the achievable level of separation power between different signal spin-parity hypotheses. While precise prediction of spin-parity separation significances also requires detailed simulation, as long as the phase-space of the discriminating observables is well-modeled, such predictions are less sensitive to details of the analysis once a given signal significance is observed.

We present results for the expected separation significance between the SM Higgs boson scenario (0_m^+) and various J^P and coupling hypotheses defined in Table I for a fixed hypothesis of a signal excess, which we take to be 5σ for the SM Higgs-like resonance. The performance quoted in Table II follows from the studies presented in the following subsections and can be interpreted in terms of integrated luminosity and pp collision energy at the LHC for each of the three channels $X \rightarrow ZZ$, WW , and $\gamma\gamma$. We observe that a simple scaling rule, significance $\sim \sqrt{L}$, is a very good approximation in these studies as long as the uncertainties are dominated by statistical errors.

We use an extended maximum-likelihood (ML) fit [19] to extract simultaneously the signal and background yields. The likelihood is defined as

$$\mathcal{L}_k = \exp(-n_{\text{sig}} - n_{\text{bkg}}) \prod_i (n_{\text{sig}} \times \mathcal{P}_{\text{sig}}^k(\mathbf{x}_i; \boldsymbol{\alpha}; \boldsymbol{\beta}) + n_{\text{bkg}} \times \mathcal{P}_{\text{bkg}}(\mathbf{x}_i; \boldsymbol{\beta})) , \quad (22)$$

where n_{sig} is the number of signal events, n_{bkg} is the number of background events and $\mathcal{P}(\mathbf{x}_i; \boldsymbol{\alpha}; \boldsymbol{\beta})$ is the probability density function for background or signal for different spin hypotheses, k . Each event candidate, i , is characterized by a set of two observables $\mathbf{x}_i = (m, D)$. The signal coupling parameters are collectively denoted by $\boldsymbol{\alpha}$, and the remaining parameters by $\boldsymbol{\beta}$. The correlated (m, D) distribution is parameterized with a binned histogram (template) using simulation. The likelihood \mathcal{L}_k in Eq. (22) is evaluated independently for each spin hypothesis k . Two sets of pseudo-experiments are generated, each with same average number of signal events of a particular type embedded into the expected background.

Examples of distributions of $-2\ln(\mathcal{L}_1/\mathcal{L}_2)$ are shown for a large number of generated experiments in Fig. 3, where one of the signal types is chosen to be the SM Higgs boson. The probability for an alternative signal to produce a

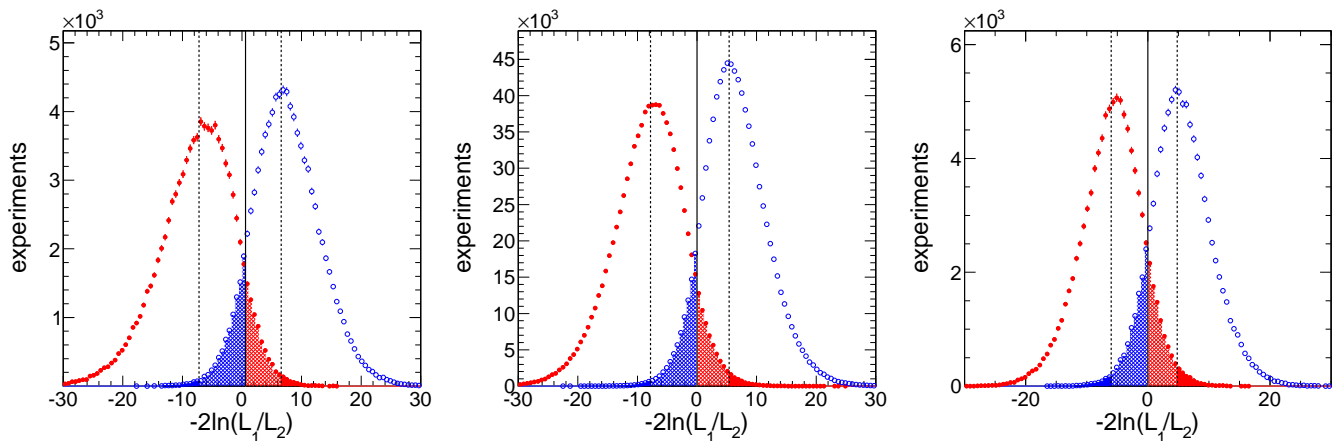


FIG. 3: Distributions of $-2\ln(\mathcal{L}_1/\mathcal{L}_2)$ with the likelihood \mathcal{L}_k evaluated for two models and shown for a large number of generated experiments in the analysis of $X \rightarrow ZZ$ (left), WW (middle), and $\gamma\gamma$ (right). The models shown are the SM Higgs boson 0^+ (red solid points) and the pseudoscalar 0^- for ZZ or the graviton-like 2_m^+ for WW and $\gamma\gamma$ (blue open points). The scenarios correspond to those shown in Table II.

value of $-2\ln(\mathcal{L}_1/\mathcal{L}_2)$ below the median value for the SM Higgs boson hypothesis is taken as the one-sided Gaussian probability and interpreted as the number of Gaussian standard deviations, \mathcal{S} . The value of \mathcal{S} corresponds to an effective separation between the two distributions in the symmetric case, or equivalently to the expected separation between the two hypotheses. However, a certain amount of asymmetry between the distributions is possible, as we note in some cases below, and the expected significance of separating type 2 signal from type 1 may differ from separation of type 1 from type 2. An approximate average of the two values could be obtained from the point beyond which the right-side tail of the left histogram and the left-side tail of the right histogram have equal areas (corresponding to $\mathcal{S}/2$). We choose to quote the first of the three values as more relevant for separation of alternative hypotheses from the SM Higgs boson. A similar technique can be employed for the significance calculation of the signal excess over background. Below we discuss details of the analysis methods that are particular to each channel.

A. $X \rightarrow ZZ$

In the $X \rightarrow ZZ \rightarrow 4\ell$ channel, the dominant background is the continuous production of $Z\gamma^*/ZZ$ ⁵. The ZZ production cross section is comparable to that of the SM Higgs boson in the four-lepton invariant mass window comparable to detector resolution. Loose selection requirements are applied to simulated signal and $q\bar{q} \rightarrow ZZ$ background events to model detector effects of CMS and ATLAS. For lepton track transverse momentum, we apply Gaussian random smearing with an rms $\Delta p_T = 0.014 \times p_T$ (GeV) for 90% of the core of the distribution and a wider smearing for the 10% tail. Leptons are required to have pseudo-rapidity in the range $|\eta| < 2.4$ and p_T greater than 7 GeV. In addition, leptons with the highest and next-to-highest transverse momentum are required to also have $p_T > 20$ and 10 GeV, respectively. To reject the non- ZZ background, the invariant masses of the di-lepton pairs are required to satisfy $50 < m_1 < 120$ GeV and $12 < m_2 < 120$ GeV, where $m_1 > m_2$. The overall ZZ rate is then scaled to be consistent with the total background observed in LHC experiments, including Drell-Yan and top events with jets faking leptons. We do not attempt to model this instrumental background shape and implicitly assume that shapes are well-modeled by $q\bar{q} \rightarrow ZZ$ events. Only events with $110 < m_{4\ell} < 160$ GeV are considered in the final analysis. The number of signal events after all selections is 0.8 events/fb⁻¹, while the number of background events is 1.9 events/fb⁻¹. Using only the $m_{4\ell}$ shape of signal and background, we find an expected significance of 3.3σ with 10 fb⁻¹ of data, comparable to that observed at the LHC⁶.

As was pointed out earlier in Ref. [19, 21], using full kinematic information in the $X \rightarrow ZZ$ channel improves signal-to-background separation by about 20% compared to a one-dimensional analysis of the invariant mass $m_{4\ell}$. This has been exploited by the CMS experiment in the discovery of the new boson [2]. One can perform either

⁵ We will collectively refer to these two processes as ZZ in what follows.

⁶ We disregard the difference between the 7 and 8 TeV collision energies of LHC for simplicity.

a multidimensional fit or create a kinematic discriminant (MELA) [2, 23] which is constructed from the ratio of probabilities for signal and background hypotheses

$$D_{\text{bkg}} = \left[1 + \frac{\mathcal{P}_{\text{sig}}(m_{4\ell}; m_1, m_2, \mathbf{\Omega})}{\mathcal{P}_{\text{bkg}}(m_{4\ell}; m_1, m_2, \mathbf{\Omega})} \right]^{-1}. \quad (23)$$

Here \mathcal{P}_{sig} and \mathcal{P}_{bkg} are the probabilities, as a function of masses m_i and angular observables $\mathbf{\Omega}$ for a given value of invariant mass $m_{4\ell}$, as defined in Eq. (5), for the SM Higgs boson signal and ZZ background, respectively. Although analytic computation of the matrix element for continuum ZZ production [21] exists, it neglects the $Z\gamma^*$ process and therefore it can not yet be applied to the region below $m_{4\ell} \sim 180$ GeV. Instead, we use a large sample of POWHEG simulated events to fill a multi-dimensional histogram (template), where the most important correlations between up to three observables are taken into account.

The above approach to background rejection is illustrated in Fig. 4, where we plot $m_{4\ell}$ and D_{bkg} , which are mostly uncorrelated in the small $m_{4\ell}$ region considered. As shown in Fig. 4, for a wide range of different signal spin-parity hypotheses, the D_{bkg} distributions do not differ considerably. However, all signal distributions of D_{bkg} differ considerably from background. We confirm that significance of the signal observation in the two-dimensional analysis of $(m_{4\ell}, D_{\text{bkg}})$ increases by more than 20% compared to a one-dimensional analysis of the invariant mass $m_{4\ell}$. To simplify the fitting model, in the rest of the paper we will not use the additional background suppression power of the D_{bkg} observable but we note that the effective significance can be increased by either including D_{bkg} in the multivariate fit, or, equivalently, using information contained in D_{bkg} in the fit.

Separation between different spin-parity scenarios of the observed resonance can also be obtained using kinematic

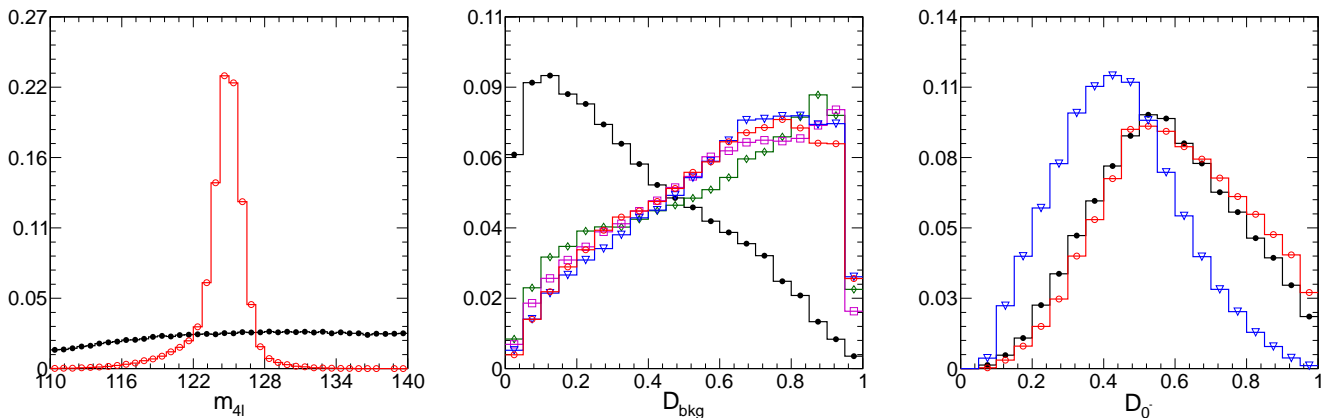


FIG. 4: Distributions of $m_{4\ell}$ (left), D_{bkg} (middle), and D_{0^-} (right) in the $X \rightarrow ZZ$ analysis for the non-resonant ZZ background (black solid circles), and four signal hypotheses: SM Higgs boson (red open circles), 0^- (magenta squares), 2_m^+ (blue triangles), and 2_h^+ (green diamonds). Not all signal hypotheses are shown on all plots. The mass range $120 < m_{4\ell} < 130$ GeV is shown in the D distributions.

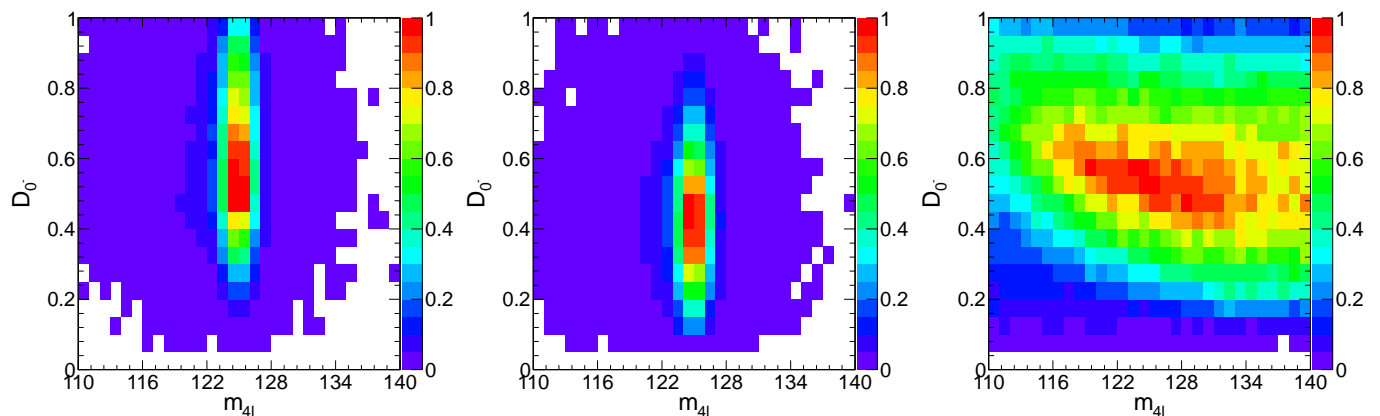


FIG. 5: Template distributions of D_{0^-} versus $m_{4\ell}$ in the $X \rightarrow ZZ$ analysis for the SM Higgs boson (left), pseudoscalar resonance (middle), and non-resonant ZZ background (right).

information. We can re-write Eq. (23) as

$$D_{J_x^P} = \left[1 + \frac{\mathcal{P}_1(m_{4\ell}; m_1, m_2, \Omega)}{\mathcal{P}_2(m_{4\ell}; m_1, m_2, \Omega)} \right]^{-1}. \quad (24)$$

where \mathcal{P}_1 and \mathcal{P}_2 are the probabilities as defined in Eq. (5), for two different hypotheses of spin-parity and tensor structure of interactions of the signal resonance. Equation (24) is indeed the optimal way to combine all relevant kinematic information into a single observable $D_{J_x^P}$ for separating the SM Higgs boson scenario from other J_x^P hypotheses without loss of information.

As an example, in the right plot of Fig. 4 we show a kinematic discriminant D_{0^-} optimized for separating 0_m^+ and 0^- signal hypotheses. D_{0^-} is calculated in Eq. (24) with \mathcal{P}_2 taken as the probability density for 0^- . Since $m_{4\ell}$ is still the most powerful observable to discriminate any type of signal from the background, we perform a two-dimensional fit of $(m_{4\ell}, D_{0^-})$. The probability densities for signal and background are parameterized as two-dimensional template histograms using simulation, as shown in Fig. 5.

In the scenario described above, with an expected SM Higgs boson signal significance of 3.3σ with 10 fb^{-1} of data, we estimate an average separation of 1.9σ between the 0_m^+ and 0^- signal hypotheses. Equivalently, assuming that the integrated luminosity is high enough to ensure 5σ signal-to-background separation, the average expected separation of 0_m^+ and 0^- is 2.9σ , see Fig. 3. This and other results for several other signal hypotheses are shown in Table II. We find the 0_m^+ and 0^- separation results consistent with those predicted by CMS [38], taking into account the assumed signal significance (expected versus observed).

The separation power depends on information contained in kinematic distributions; we show illustrative examples in Figs. 3, 11, and 12. For example, separation of the SM Higgs boson hypothesis from 0^- is better than from 2_m^+ since a number of mass and angular distributions are more distinct. Also, we note that both 2_h^+ and 2_h^- are even more different from 0_m^+ than any other hypothesis considered. One of the kinematic distributions that shows important differences between the SM Higgs boson and the pseudoscalar, as well as between the SM Higgs boson and 2_h^+ or 2_h^- , is the low-mass tail of m_1 distribution, see the left plot in Fig. 2. As shown in Ref. [38], there is a rather large fraction of the $X \rightarrow ZZ$ events in CMS with both Z 's off-shell. If this feature persists in data, it may reveal contributions of momentum-dependent couplings shown in Eqs. (9) and (18). We note that a particular feature which may enhance the m_1 tail considerably, as shown for the 2_h^+ hypothesis in Fig. 3, is the presence of a large power of the parameter x in Eq. (21). In turn, the appearance of this parameter is related to the terms c_2 and c_3 in A_{00} which are sensitive to $g_4^{(2)}$ coupling.

We comment about an interesting feature in Table II. On general grounds one can expect that significance of hypotheses separation between two types of signal to be smaller than the observation significance of the signal. However, in a situation when the kinematic discriminant itself provides substantial background rejection power, significance of the observation of the alternative signal may become higher than that for the SM Higgs-like resonance. This phenomenon occurs in the study of 2_h^+ and 2_h^- hypotheses, where the m_1 mass distribution becomes a particularly powerful discriminating observable. As a result, for the corresponding signal types, $D_{2_h^+}$ and $D_{2_h^-}$ may become even stronger background rejection observables than $m_{4\ell}$. We do not see this in Fig. 4 because the SM Higgs boson hypothesis is used for the computation of D_{bkg} , but an alternative signal hypothesis could have been considered as well. The m_1 -distribution then also leads to a very strong signal hypothesis separation, approaching the values of 5σ for SM Higgs boson versus 2_h^+ and 2_h^- in Table II.

We note that analysis of the spin-parity hypotheses should not be limited to just discrete hypothesis testing. In Ref. [19] we showed how a continuous spectrum of parameters can be obtained from a multidimensional fit. As an intermediate step, one could consider determination of the fraction of a certain component in a mixed state. For the spin-zero particle, this can be modeled by non-vanishing $g_1^{(0)}$ and $g_4^{(0)}$ couplings in Eq. (9). We note that, in this scenario, there is an interference term in the amplitude which is correctly described by our simulation. Results presented in Table II can be used to illustrate the typical precision on the fraction by dividing the full range between the two extreme hypotheses by the number of standard deviations between them. For example, this implies that by the end of the 8 TeV run, the LHC experiments may be able to constrain an approximately 50% admixture of the 0^- and 0^+ states at 95% confidence level.

B. $X \rightarrow WW$

Compared to the ZZ final state, the $X \rightarrow WW \rightarrow 2\ell 2\nu$ channel is expected to have a larger rate due to a larger branching fraction of $WW \rightarrow 2\ell 2\nu$, provided that decay rates $X \rightarrow ZZ$ and $X \rightarrow WW$ are comparable. However the analysis suffers from large backgrounds and the fact that neutrino momenta cannot be reconstructed. In place of the four-lepton invariant mass, the transverse mass defined as $m_T = (2p_T^{\ell\ell} E_T^{\text{miss}} (1 - \cos \Delta\phi_{\ell\ell - E_T^{\text{miss}}}))^{1/2}$, where $\Delta\phi_{\ell\ell - E_T^{\text{miss}}}$

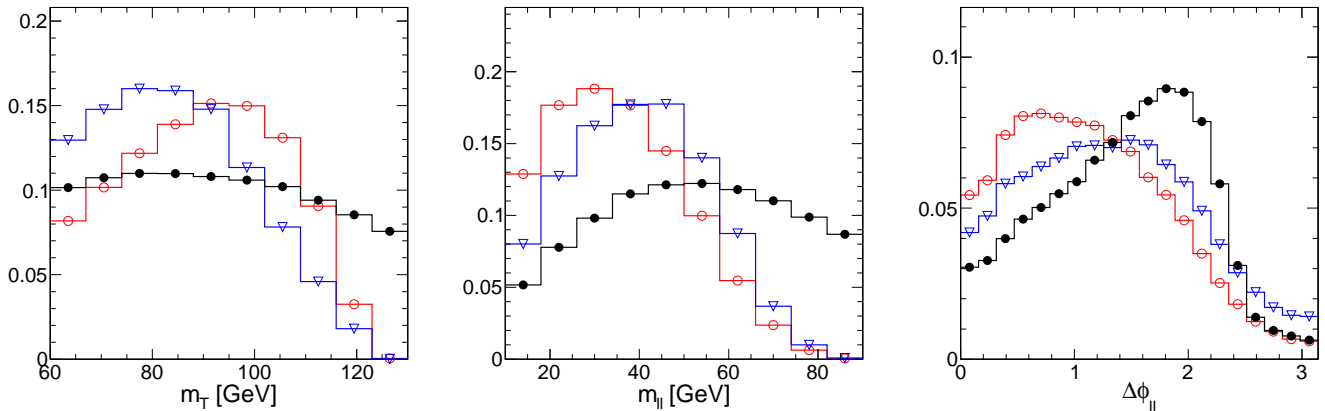


FIG. 6: Distributions of m_T (left), $m_{\ell\ell}$ (middle), and $\Delta\phi_{\ell\ell}$ (right) in the $X \rightarrow WW$ analysis for the non-resonant WW background (black solid circles), SM Higgs boson (red open circles), and a spin-two resonance in the 2_m^+ model (blue triangles).

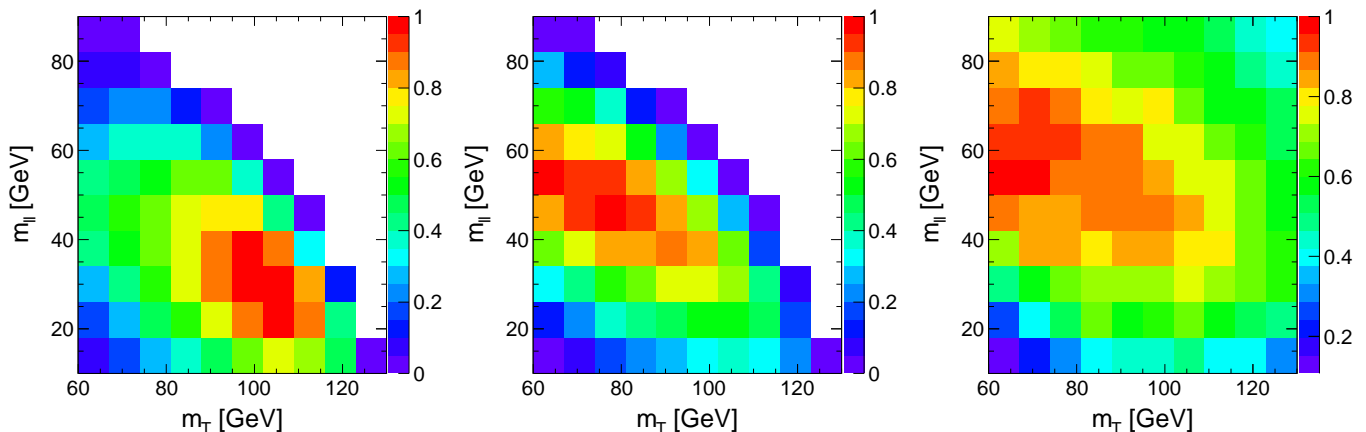


FIG. 7: Template distribution of $m_{\ell\ell}$ versus m_T in the $X \rightarrow WW$ analysis for the SM Higgs boson (left), spin-two resonance hypothesis 2_m^+ (middle), and non-resonant WW background (right).

is the angle between the direction of the di-lepton pair and the missing energy E_T^{miss} vector in the transverse plane, is exploited to disentangle signal from background [1, 2]. In our simplified study E_T^{miss} is calculated from the 2ν momentum. The one-jet $e\mu$ and zero-jet same-flavor categories only contribute to the signal sensitivity at the 10% level because of larger backgrounds from top-quark decays and Drell-Yan production, respectively [1, 2]. Therefore, we only select events with different lepton flavors ($e\mu$) and little jet activity to enhance signal-to-background ratio, so all events with jets with transverse energy greater than 30 GeV are rejected. In this category, the main background comes from the non-resonant WW production [1, 2]. To further reject the reducible backgrounds such as Drell-Yan and $W + \text{jets}/\gamma$ processes, we require $p_T > 20(10)$ GeV for the leading (sub-leading) lepton, $p_T^{\ell\ell} > 30$ GeV for the di-lepton system, $E_T^{\text{miss}} > 20$ GeV, $60 < m_T < 130$ GeV, and $10 < m_{\ell\ell} < 90$ GeV.

We estimate the expected number of signal and WW background events after this selection by extrapolating the expected yields in the signal regions used in Ref. [2] to the signal region defined above using simulation. The estimated number of SM Higgs boson events is 13 per fb^{-1} . The number of non-resonant WW background events is estimated to be 104 per fb^{-1} . We also assume that continuum WW production gives two-thirds of the total background and that kinematic distributions of the non- WW backgrounds are the same as the ones of the WW background. We cross-check this estimation using the signal region used in Ref. [1] and find consistent results. To extract the expected significance for separating different signal hypotheses \mathcal{S} , we construct a two-dimensional template based on two observables $(m, D) = (m_T, m_{\ell\ell})$; this is illustrated in Figs. 6 and 7. We have also considered other observables, such as the azimuthal angle $\Delta\phi_{\ell\ell}$ between the two leptons and found smaller separation compared to the case when $m_{\ell\ell}$ is used. On the other hand, since there is large correlation between $\Delta\phi_{\ell\ell}$ and $m_{\ell\ell}$, using three observables in the fit is not expected to increase the significance of the separation much.

Using this simplified background model, we estimate the expected significance for distinguishing the SM Higgs

boson hypothesis from the background with 10 fb^{-1} using either the single observable $m_{\ell\ell}$ or the two observables m_T and $m_{\ell\ell}$. The former approach gives 2.6σ separation from the background, similar to results of the LHC [1, 2], while the latter gives 3.5σ which is an improvement of 35%. We follow the procedure outlined for the $X \rightarrow ZZ$ analysis above and present the results in Fig. 3 and Table II. We find good separation between the SM Higgs boson and the 2_m^+ hypotheses in particular, where this channel may have an advantage over the $X \rightarrow ZZ$ channel. The reason for better performance of the WW channel for 2_m^+ separation is the larger value of parameter A_f defined in the Appendix A, which enters the angular distributions in Eq. (A1). As a consequence, there are larger azimuthal angular variations which are illustrated in Figs. 2, 12, and 13.

C. $X \rightarrow \gamma\gamma$

In the inclusive $X \rightarrow \gamma\gamma$ decay analysis, all information about the couplings is contained in the $\cos\theta^*$ distribution. The distribution is flat for a spin-zero resonance, while for a spin-two it is a normalized second degree polynomial in $\cos^2\theta^*$ which requires two independent parameters. Non-zero values of either parameter would be an unambiguous sign of a spin-two (or in principle higher spin) resonance. However, relating these coefficients to general couplings will have many ambiguities which are not generally present in the ZZ and WW channels. Indeed, the spin-two $X \rightarrow \gamma\gamma$

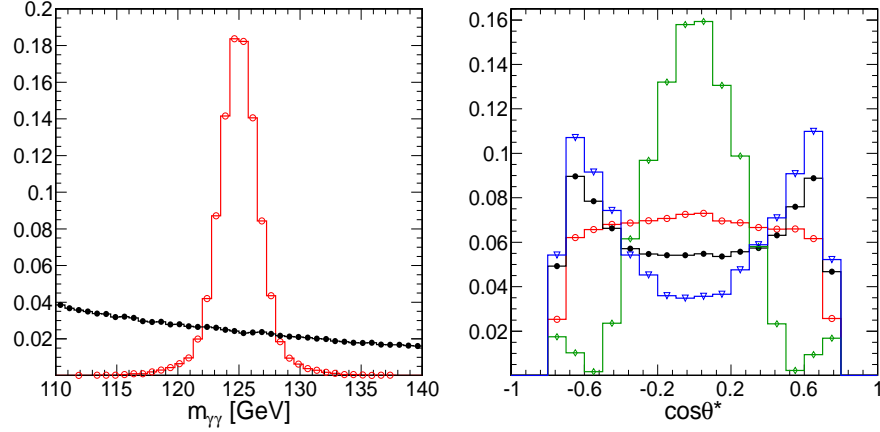


FIG. 8: Distributions of $m_{\gamma\gamma}$ (left) and $\cos\theta^*$ (right) in the $X \rightarrow \gamma\gamma$ analysis for the non-resonant $\gamma\gamma$ background (black solid circles), SM Higgs boson (red open circles), the spin-two resonance in the 2_m^+ model (blue triangles) and 2_h^+ or 2_h^- models (green diamonds). The mass range $120 < m_{\gamma\gamma} < 130$ GeV is shown in the $\cos\theta^*$ plot for background.

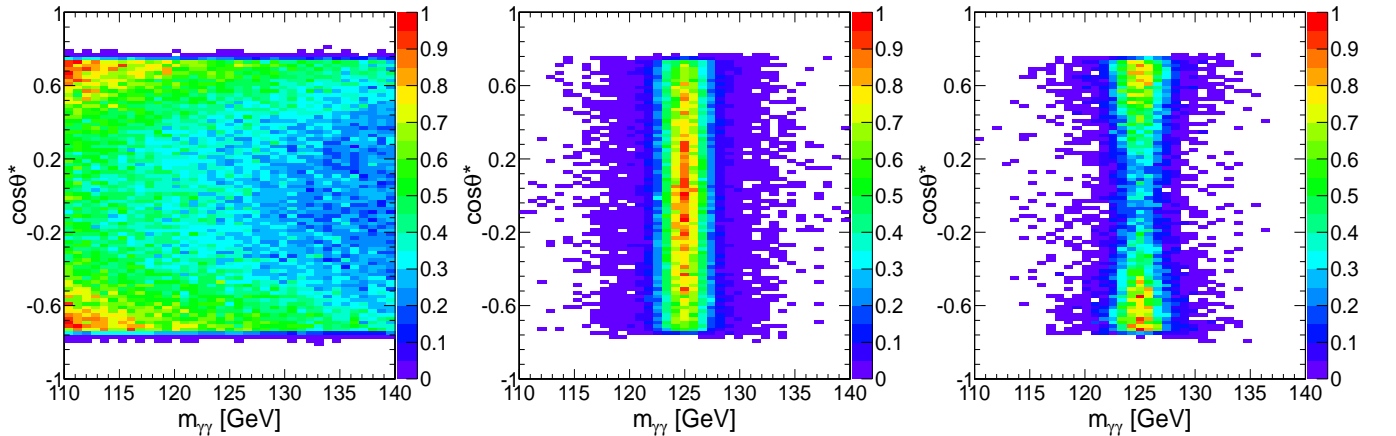


FIG. 9: Template distributions of $\cos\theta^*$ versus $m_{\gamma\gamma}$ in the $X \rightarrow \gamma\gamma$ analysis for the background (left), SM Higgs boson (middle), and spin-two resonance hypothesis 2_m^+ (right).

angular distribution reads

$$\begin{aligned} \frac{16 d\Gamma(X_{J=2} \rightarrow \gamma\gamma)}{5 \Gamma d \cos \theta^*} &= (2 - 2f_{z1} + f_{z2}) - 6(2 - 4f_{z1} - f_{z2}) \cos^2 \theta^* + 3(6 - 10f_{z1} - 5f_{z2}) \cos^4 \theta^* \\ &+ f_{+-} \{ (2 + 2f_{z1} - 7f_{z2}) + 6(2 - 6f_{z1} + f_{z2}) \cos^2 \theta^* - 5(6 - 10f_{z1} - 5f_{z2}) \cos^4 \theta^* \} \\ &\propto 1 + A \times \cos^2 \theta^* + B \times \cos^4 \theta^* , \end{aligned} \quad (25)$$

where f_{++} , f_{--} , and $f_{-+} = f_{+-}$ are fractions of transverse amplitudes in the decay, and f_{z1} and f_{z2} are polarization fractions in production, see Appendix A of Ref. [19] for more details. The special case of the minimal coupling in both production and decay corresponds to $f_{z1} + f_{z2} = 1$ and $f_{+-} = f_{-+} = 1/2$. In this case, one obtains $(1 + 6 \cos^2 \theta^* + \cos^4 \theta^*)$ for the gg production mechanism with $f_{z2} = 1$ and $(1 - \cos^4 \theta^*)$ for the $q\bar{q}$ production mechanism with $f_{z1} = 1$. The ideal distributions in Eq. (25) are shown together with generated events in Fig. 2. These distributions are identical for the 2_h^+ and 2_h^- hypotheses.

For illustration purposes, we proceed with the discussion of a simplified analysis. The acceptance thresholds, chosen to be similar to those used in LHC analyses, are $E_T^1 > m_{\gamma\gamma}/3$ and $E_T^2 > m_{\gamma\gamma}/4$ for the first and second photons, respectively. We apply η -dependent Gaussian random smearing to photon cluster energy which varies between between 1% in the central pseudorapidity region and 6% in the forward region. Photons must be inside the calorimeter acceptance $|\eta| < 2.5$ and outside the crack region $1.44 < |\eta| < 1.57$, similarly to the CMS experiment. Considering the mass window $110 < m_{\gamma\gamma} < 140$ GeV, we estimate the expected number of signal and background events based on Refs. [1, 2] to be 22 and 3515 per fb^{-1} , respectively. To extract the expected separation significance between different signal spin-parity hypotheses \mathcal{S} , we construct a two-dimensional template based on $(m, D) = (m_{\gamma\gamma}, \cos \theta^*)$ shown in Figs. 8 and 9. The loss of events at large values of $|\cos \theta^*|$ limits the precision of polarization measurements and is due to p_T and η selection requirements. Similar effects appear in the analysis of the Drell-Yan process, as discussed for example in Ref. [39]. We rely on the shapes of the distributions after the above kinematic selection, and the normalization is taken from data. Using two-dimensional $(m_{\gamma\gamma}, \cos \theta^*)$ templates, we obtain 2.7σ significance with 10 fb^{-1} , which is similar to the LHC results expected for the SM Higgs boson [1, 2].

We find good separation between the SM Higgs boson hypothesis and the spin-two models considered, as can be seen in Fig. 3 and in Table II. However, since just one angle is available in the analysis, the separation power may be weak or absent for other models where the $\cos \theta^*$ distribution is close to flat.

V. SUMMARY AND CONCLUSION

We have described a framework to determine the spin, parity, and general tensor structure of interactions of the new boson observed at the LHC. We consider a variety of Lorentz structures for spin-parity hypothesis testing that go beyond the minimal couplings expected for the SM Higgs boson or the graviton-like interactions of a spin-two boson. The full analytical calculation of angular and mass dependence of the decay amplitude $X \rightarrow V^*V^*$ allows the most general analysis of a resonance with any integer spin J . A Monte Carlo simulation of the process $pp \rightarrow X \rightarrow V^*V^*$, with $V = Z, W$, and γ , with off-shell electroweak gauge bosons, all spin correlations, and general couplings enables experimental investigation of the properties of the new resonance. Both the analytic formulas and the event generator are publicly available, see Ref. [33].

We have illustrated how the spin and parity of the new boson can be tested in the processes $pp \rightarrow X \rightarrow ZZ, WW$, and $\gamma\gamma$, using simplified simulation of the background and of the detector effects at the LHC experiments. We have presented the expected significance of spin-parity hypothesis separation for several scenarios in Table II, where it is assumed that the 5σ signal-to-background separation is achieved in each channel. The linearity of the relation between the signal-to-background significance and the spin-parity signal hypothesis separation significance allows us to extrapolate expectations to different luminosity scenarios, as shown in Fig. 3 for 0^- and 2_m^+ models. We rely on the expected signal-to-background significances reported by the LHC experiments for the integrated luminosity of about 10 fb^{-1} , which we take as 3.8, 2.4, and 2.8σ in the $X \rightarrow ZZ, WW$, and $\gamma\gamma$ channels, respectively [2]. In Table III we show examples of hypothesis separation expectations, per each LHC experiment, by the end of the 8 TeV LHC run, assuming 35 fb^{-1} of integrated luminosity.

We would also like to comment on some other potential final states in the decay of the new boson, such as $Z\gamma$ and fermion-antifermion final states. Since no significant excess of events in these final states has been observed, we leave detailed discussion of these final states to later work. However, the techniques discussed in this paper are applicable to them as well. For example, analysis of associated production $q\bar{q} \rightarrow Z^* \rightarrow ZX \rightarrow (\ell^-\ell^+)(b\bar{b})$ or $(\ell^-\ell^+)(\tau^-\tau^+)$, and similarly $q\bar{q}' \rightarrow W^* \rightarrow WX$, would follow the same formalism as discussed above. In the above processes, the angular distributions of decay products should allow discrimination between the spin and coupling hypotheses for both XVV and $Xf\bar{f}$. For a spin-zero X decay, the fermion angular distributions are flat; for a spin-one X , the

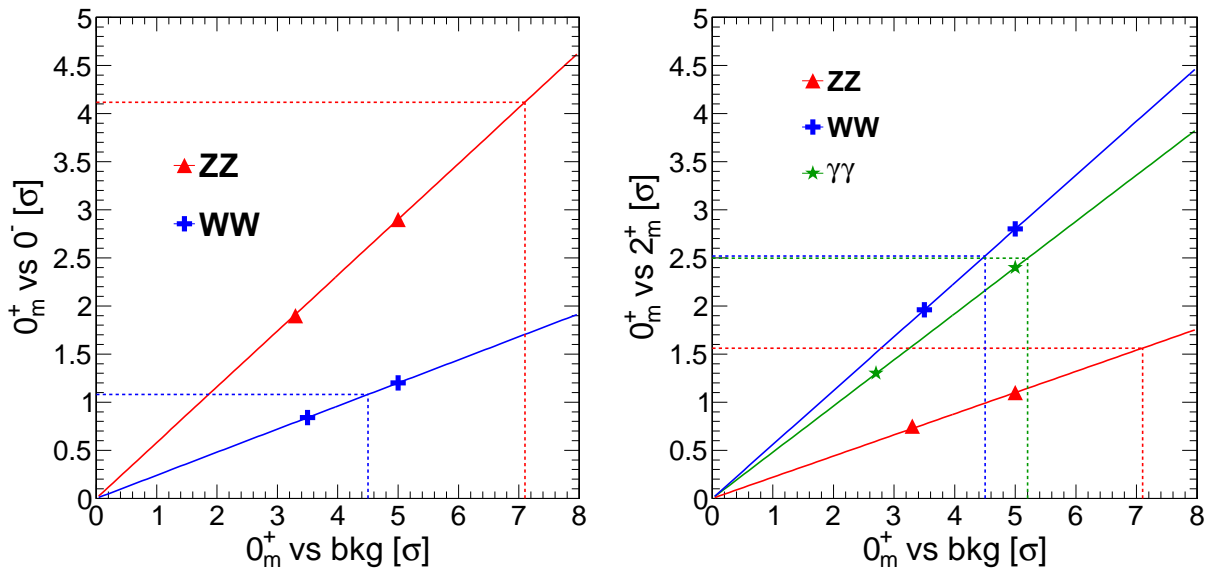


FIG. 10: Expected hypotheses separation significance versus signal observation significance for the SM Higgs boson versus 0^- (left) and 2_m^+ (right) hypotheses. Points show two luminosity scenarios tested with generated experiments and expectations are extrapolated linearly to other significance scenarios. Dashed lines indicate what might be expected with 35 fb^{-1} of data at one LHC experiment.

angular distributions are similar to those in Eq. (A1) with $J = 1$; and for a spin-two X , the angular distributions can be obtained in a similar manner. The angular distributions for general couplings in the decay $X \rightarrow f\bar{f}$ can be obtained from Ref. [19].

In view of the importance of the discovery of the new boson for particle physics, it is important to confront all theoretical assumptions about its properties against experimental facts. The results presented in this paper point towards a realistic possibility that by the end of the 8 TeV run of the LHC, extreme hypotheses about spin and parity of the new boson can be experimentally excluded. However, it will be much harder to exclude contributions of anomalous couplings of the Higgs bosons to gauge bosons if they are smaller than ten percent of the SM couplings. For that, a significantly larger dataset will be required and multivariate fitting techniques [19] will help to achieve this goal. Nonetheless, if the nature of the new boson discovered at the LHC is exotic, there is a good chance to determine this already in the coming year.

Acknowledgments: Several of us would like to thank CMS collaboration colleagues for feedback during the working group presentations of this analysis, and in particular Serguei Ganjour and Chia Ming Kuo for discussion of the two-photon analysis performance. This research is partially supported by US NSF under grants PHY-1100862 and PHY-1214000, and by US DOE under grants DE-AC02-06CD11357 and DE-AC02-07CH11359. We also acknowledge support from the LPC-CMS Fellows program operated through FNAL. Calculations reported in this paper were performed on the Homewood High Performance Cluster of the Johns Hopkins University.

TABLE III: Expected separation significance \mathcal{S} (Gaussian σ) between the SM Higgs boson scenario (0_m^+) and 0^- or 2_m^+ hypotheses in the analyzed channels and combined, for the scenario corresponding approximately to 35 fb^{-1} of integrated luminosity at one LHC experiment.

scenario	$X \rightarrow ZZ$	$X \rightarrow WW$	$X \rightarrow \gamma\gamma$	combined
0_m^+ vs background	7.1	4.5	5.2	9.9
0_m^+ vs 0^-	4.1	1.1	0.0	4.2
0_m^+ vs 2_m^+	1.6	2.5	2.5	3.9

Appendix A: Analytical angular distributions

In this appendix we present the general angular distribution in the production and decay of a particle X , with any integer spin J , in parton collisions $ab \rightarrow X \rightarrow V_1(q_1)V_2(q_2)$, $V_1 \rightarrow f(q_{11})\bar{f}(q_{12})$, $V_2 \rightarrow f(q_{21})\bar{f}(q_{22})$, as derived in Ref. [19] and generalized here to remove the constraint between the $A_{\alpha\beta}$ and $A_{\beta\alpha}$ amplitudes. Helicity amplitudes $A_{\alpha\beta}$ depend on the vector boson resonance masses m_1 and m_2 , as described in Eqs. (14), (17), and (21), and related formulas incorporating the couplings. We work in the rest frame of the resonance X and all angles that we use below are defined in Section II.

The amplitudes $A_{\alpha\beta}$ are, in general, complex and the angular distribution is parameterized by the magnitude of the amplitude $|A_{\alpha\beta}|$ and the phase $\phi_{\alpha\beta} = \arg(A_{\alpha\beta}/A_{00})$. The angular distribution is

$$\begin{aligned}
& \frac{\mathcal{N}_J d\Gamma_J(m_1, m_2, \cos\theta^*, \Psi, \cos\theta_1, \cos\theta_2, \Phi)}{d\cos\theta^* d\Psi d\cos\theta_1 d\cos\theta_2 d\Phi} = \\
& F_{0,0}^J(\theta^*) \times \left[4|A_{00}|^2 \sin^2\theta_1 \sin^2\theta_2 \right. \\
& \quad + |A_{++}|^2 (1 + 2A_{f_1} \cos\theta_1 + \cos^2\theta_1) (1 + 2A_{f_2} \cos\theta_2 + \cos^2\theta_2) \\
& \quad + |A_{--}|^2 (1 - 2A_{f_1} \cos\theta_1 + \cos^2\theta_1) (1 - 2A_{f_2} \cos\theta_2 + \cos^2\theta_2) \\
& \quad + 4|A_{00}||A_{++}|(A_{f_1} + \cos\theta_1) \sin\theta_1 (A_{f_2} + \cos\theta_2) \sin\theta_2 \cos(\Phi + \phi_{++}) \\
& \quad + 4|A_{00}||A_{--}|(A_{f_1} - \cos\theta_1) \sin\theta_1 (A_{f_2} - \cos\theta_2) \sin\theta_2 \cos(\Phi - \phi_{--}) \\
& \quad \left. + 2|A_{++}||A_{--}| \sin^2\theta_1 \sin^2\theta_2 \cos(2\Phi - \phi_{--} + \phi_{++}) \right] \\
& + F_{1,1}^J(\theta^*) \times \left[2|A_{+0}|^2 (1 + 2A_{f_1} \cos\theta_1 + \cos^2\theta_1) \sin^2\theta_2 \right. \\
& \quad + 2|A_{0-}|^2 \sin^2\theta_1 (1 - 2A_{f_2} \cos\theta_2 + \cos^2\theta_2) \\
& \quad + 2|A_{-0}|^2 (1 - 2A_{f_1} \cos\theta_1 + \cos^2\theta_1) \sin^2\theta_2 \\
& \quad + 2|A_{0+}|^2 \sin^2\theta_1 (1 + 2A_{f_2} \cos\theta_2 + \cos^2\theta_2) \\
& \quad + 4|A_{+0}||A_{0-}|(A_{f_1} + \cos\theta_1) \sin\theta_1 (A_{f_2} - \cos\theta_2) \sin\theta_2 \cos(\Phi + \phi_{+0} - \phi_{0-}) \\
& \quad \left. + 4|A_{0+}||A_{-0}|(A_{f_1} - \cos\theta_1) \sin\theta_1 (A_{f_2} + \cos\theta_2) \sin\theta_2 \cos(\Phi + \phi_{0+} - \phi_{-0}) \right] \\
& + F_{1,-1}^J(\theta^*) \times \left[4|A_{+0}||A_{0+}|(A_{f_1} + \cos\theta_1) \sin\theta_1 (A_{f_2} + \cos\theta_2) \sin\theta_2 \cos(2\Psi - \phi_{+0} + \phi_{0+}) \right. \\
& \quad + 4|A_{+0}||A_{-0}| \sin^2\theta_1 \sin^2\theta_2 \cos(2\Psi - \Phi - \phi_{+0} + \phi_{-0}) \\
& \quad + 4|A_{0-}||A_{0+}| \sin^2\theta_1 \sin^2\theta_2 \cos(2\Psi + \Phi - \phi_{0-} + \phi_{0+}) \\
& \quad \left. + 4|A_{0-}||A_{-0}|(A_{f_1} - \cos\theta_1) \sin\theta_1 (A_{f_2} - \cos\theta_2) \sin\theta_2 \cos(2\Psi - \phi_{0-} + \phi_{-0}) \right] \\
& + F_{2,2}^J(\theta^*) \times \left[|A_{+-}|^2 (1 + 2A_{f_1} \cos\theta_1 + \cos^2\theta_1) (1 - 2A_{f_2} \cos\theta_2 + \cos^2\theta_2) \right. \\
& \quad \left. + |A_{-+}|^2 (1 - 2A_{f_1} \cos\theta_1 + \cos^2\theta_1) (1 + 2A_{f_2} \cos\theta_2 + \cos^2\theta_2) \right] \\
& + F_{2,-2}^J \left[2|A_{+-}||A_{-+}| \sin^2\theta_1 \sin^2\theta_2 \cos(4\Psi - \phi_{+-} + \phi_{-+}) \right] \\
& - F_{0,1}^J(\theta^*) \times \left[4\sqrt{2}|A_{00}||A_{+0}|(A_{f_1} + \cos\theta_1) \sin\theta_1 \sin^2\theta_2 \cos(\Psi - \Phi/2 - \phi_{+0}) \right. \\
& \quad + 4\sqrt{2}|A_{00}||A_{0-}| \sin^2\theta_1 (A_{f_2} - \cos\theta_2) \sin\theta_2 \cos(\Psi + \Phi/2 - \phi_{0-}) \\
& \quad + 2\sqrt{2}|A_{--}||A_{+0}| \sin^2\theta_1 (A_{f_2} - \cos\theta_2) \sin\theta_2 \cos(-\Psi + 3\Phi/2 + \phi_{+0} - \phi_{--}) \\
& \quad + 2\sqrt{2}|A_{--}||A_{0-}|(A_{f_1} - \cos\theta_1) \sin\theta_1 (1 - 2A_{f_2} \cos\theta_2 + \cos^2\theta_2) \cos(-\Psi + \Phi/2 + \phi_{0-} - \phi_{--}) \\
& \quad + 2\sqrt{2}|A_{++}||A_{+0}|(1 + 2A_{f_1} \cos\theta_1 + \cos^2\theta_1) (A_{f_2} + \cos\theta_2) \sin\theta_2 \cos(\Psi + \Phi/2 - \phi_{+0} + \phi_{++}) \\
& \quad \left. + 2\sqrt{2}|A_{++}||A_{0-}|(A_{f_1} + \cos\theta_1) \sin\theta_1 \sin^2\theta_2 \cos(\Psi + 3\Phi/2 - \phi_{0-} + \phi_{++}) \right] \\
& - F_{0,-1}^J(\theta^*) \times \left[4\sqrt{2}|A_{00}||A_{0+}| \sin^2\theta_1 (A_{f_2} + \cos\theta_2) \sin\theta_2 \cos(\Psi + \Phi/2 + \phi_{+0}) \right. \\
& \quad + 4\sqrt{2}|A_{00}||A_{-0}|(A_{f_1} - \cos\theta_1) \sin\theta_1 \sin^2\theta_2 \cos(\Psi - \Phi/2 + \phi_{-0}) \\
& \quad \left. + 2\sqrt{2}|A_{--}||A_{0+}|(A_{f_1} - \cos\theta_1) \sin\theta_1 \sin^2\theta_2 \cos(\Psi + 3\Phi/2 + \phi_{0+} - \phi_{--}) \right]
\end{aligned}$$

$$\begin{aligned}
& + 2\sqrt{2}|A_{--}||A_{-0}|(1 - 2A_{f_1} \cos \theta_1 + \cos^2 \theta_1)(A_{f_2} - \cos \theta_2) \sin \theta_2 \cos(\Psi + \Phi/2 + \phi_{-0} - \phi_{--}) \\
& + 2\sqrt{2}|A_{++}||A_{0+}|(A_{f_1} + \cos \theta_1) \sin \theta_1(1 + 2A_{f_2} \cos \theta_2 + \cos^2 \theta_2) \cos(\Psi - \Phi/2 + \phi_{0+} - \phi_{++}) \\
& + 2\sqrt{2}|A_{++}||A_{-0}| \sin^2 \theta_1(A_{f_2} + \cos \theta_2) \sin \theta_2 \cos(-\Psi + 3\Phi/2 - \phi_{-0} + \phi_{++}) \Big] \\
& + F_{0,2}^J(\theta^*) \times \Big[4|A_{00}||A_{+-}|(A_{f_1} + \cos \theta_1) \sin \theta_1(A_{f_2} - \cos \theta_2) \sin \theta_2 \cos(2\Psi - \phi_{+-}) \\
& + 2|A_{--}||A_{+-}| \sin^2 \theta_1(1 - 2A_{f_2} \cos \theta_2 + \cos^2 \theta_2) \cos(2\Psi - \Phi + \phi_{--} - \phi_{+-}) \\
& + 2|A_{++}||A_{+-}|(1 + 2A_{f_1} \cos \theta_1 + \cos^2 \theta_1) \sin^2 \theta_2 \cos(2\Psi + \Phi + \phi_{++} - \phi_{+-}) \Big] \\
& + F_{0,-2}^J(\theta^*) \times \Big[4|A_{00}||A_{-+}|(A_{f_1} - \cos \theta_1) \sin \theta_1(A_{f_2} + \cos \theta_2) \sin \theta_2 \cos(2\Psi + \phi_{-+}) \\
& + 2|A_{--}||A_{-+}|(1 - 2A_{f_1} \cos \theta_1 + \cos^2 \theta_1) \sin^2 \theta_2 \cos(2\Psi + \Phi - \phi_{--} + \phi_{-+}) \\
& + 2|A_{++}||A_{-+}| \sin^2 \theta_1(1 + 2A_{f_2} \cos \theta_2 + \cos^2 \theta_2) \cos(2\Psi - \Phi - \phi_{++} + \phi_{-+}) \Big] \\
& - F_{1,2}^J(\theta^*) \times \Big[2\sqrt{2}|A_{+0}||A_{+-}|(1 + 2A_{f_1} \cos \theta_1 + \cos^2 \theta_1)(A_{f_2} - \cos \theta_2) \sin \theta_2 \cos(\Psi + \Phi/2 + \phi_{+0} - \phi_{+-}) \\
& + 2\sqrt{2}|A_{0-}||A_{+-}|(A_{f_1} + \cos \theta_1) \sin \theta_1(1 - 2A_{f_2} \cos \theta_2 + \cos^2 \theta_2) \cos(\Psi - \Phi/2 + \phi_{0-} - \phi_{+-}) \\
& + 2\sqrt{2}|A_{0+}||A_{-+}|(A_{f_1} - \cos \theta_1) \sin \theta_1(1 + 2A_{f_2} \cos \theta_2 + \cos^2 \theta_2) \cos(-\Psi + \Phi/2 + \phi_{0+} - \phi_{-+}) \\
& + 2\sqrt{2}|A_{-0}||A_{-+}|(1 - 2A_{f_1} \cos \theta_1 + \cos^2 \theta_1)(A_{f_2} + \cos \theta_2) \sin \theta_2 \cos(\Psi + \Phi/2 + \phi_{-0} - \phi_{-+}) \Big] \\
& - F_{1,-2}^J(\theta^*) \times \Big[2\sqrt{2}|A_{+0}||A_{-+}| \sin^2 \theta_1(A_{f_2} + \cos \theta_1) \sin \theta_2 \cos(3\Psi - \Phi/2 - \phi_{+0} + \phi_{-+}) \\
& + 2\sqrt{2}|A_{0-}||A_{-+}|(A_{f_1} - \cos \theta_1) \sin \theta_1 \sin^2 \theta_2 \cos(3\Psi + \Phi/2 - \phi_{0-} + \phi_{-+}) \\
& + 2\sqrt{2}|A_{0+}||A_{-+}|(A_{f_1} + \cos \theta_1) \sin \theta_1 \sin^2 \theta_2 \cos(3\Psi + \Phi/2 + \phi_{0+} - \phi_{-+}) \\
& + 2\sqrt{2}|A_{-0}||A_{-+}| \sin^2 \theta_1(A_{f_2} - \cos \theta_2) \sin \theta_2 \cos(3\Psi - \Phi/2 + \phi_{-0} - \phi_{-+}) \Big], \tag{A1}
\end{aligned}$$

where \mathcal{N}_J is the normalization constant which does not affect the angular and mass distributions. Because decays of vector bosons $V_i \rightarrow f_i \bar{f}_i$ are involved, the angular distributions depend on the parameter A_{f_i} characterizing their decay, defined as $A_f = 2\bar{g}_V^f \bar{g}_A^f / (\bar{g}_V^{f^2} + \bar{g}_A^{f^2})$ [29]. This parameter is 1 for W decays and approximately 0.15 for $Z \rightarrow \ell^- \ell^+$. Equation (A1) represents a more general version of Eq. (B1) from Ref. [19], where sign conventions are different between the two equations. Conventions for Eq. (A1) are consistent with Eqs. (2–4). The functions $F_{i,j}^J(\theta^*)$ are defined as

$$F_{i,j}^J(\theta^*) = \sum_{m=0,\pm 1,\pm 2} f_m d_{mi}^J(\theta^*) d_{mj}^J(\theta^*), \tag{A2}$$

where f_m are fractions of the X particle polarization as defined in Ref. [19]. In $q\bar{q}$ annihilation the resonance X can only be produced by $m = \pm 1$, whereas in gluon fusion $m = \pm 2$ or 0. The relative fractions of $m = \pm 2$ and 0 are determined by amplitudes in Eq. (21) which simplify in the case of couplings to two massless gluons and depend on production couplings in Eq. (18). The relative fraction of $q\bar{q} \rightarrow X$ production is denoted by $f_{q\bar{q}}$ and is determined by the ratio of cross-sections, including effects of parton structure functions. This leads to

$$\begin{aligned}
f_{+1} = f_{-1} &= \frac{f_{z1}}{2} = \frac{f_{q\bar{q}}}{2}, \\
f_{+2} = f_{-2} &= \frac{f_{z2}}{2} = (1 - f_{q\bar{q}}) \frac{|A_{+-}^{gg}|^2}{\sum_{\alpha,\beta=\pm 1} |A_{\alpha\beta}^{gg}|^2} = (1 - f_{q\bar{q}}) \frac{|A_{-+}^{gg}|^2}{\sum_{\alpha,\beta=\pm 1} |A_{\alpha\beta}^{gg}|^2}, \\
f_0 = f_{z0} &= (1 - f_{q\bar{q}}) \frac{|A_{++}^{gg}|^2 + |A_{--}^{gg}|^2}{\sum_{\alpha,\beta=\pm 1} |A_{\alpha\beta}^{gg}|^2}. \tag{A3}
\end{aligned}$$

For a spin-zero resonance $f_{q\bar{q}} = 0$ and $f_0 = 1$. For a spin-one resonance $f_{q\bar{q}} = 1$. For a spin-two resonance, generally all polarizations are possible. The minimal couplings of a spin-two resonance correspond to $f_0 = 0$. Specific examples of $F_{i,j}^J$ for $J = 0, 1, 2$ are given in Ref. [19].

Appendix B: Angular and mass distributions

We illustrate MC simulation and compare it to the derived analytical angular and mass distributions in Figs. 11 and 12 for the ZZ , and in Fig. 13 for the WW final states. The $X \rightarrow \gamma\gamma$ distributions are shown in Fig. 2.

-
- [1] ATLAS collaboration, submitted to Phys. Lett. B, arXiv:1207.7214 [hep-ex].
 - [2] CMS collaboration, submitted to Phys. Lett. B, arXiv:1207.7235 [hep-ex].
 - [3] CDF and D0 collaborations, submitted to Phys. Rev. Lett., arXiv:1207.6436 [hep-ex].
 - [4] L. D. Landau, Dokl. Akad. Nauk., USSR **60**, 207 (1948).
 - [5] C. N. Yang, Phys. Rev. **77**, 242 (1950).
 - [6] D. Carmi *et al.*, arXiv:1207:1718 [hep-ph]; P.P. Giardino *et al.*, arXiv:1207:1347 [hep-ph]; J. Ellis and T. You, arXiv:1207:1347 [hep-ph]; J. R. Espinosa *et al.*, arXiv: 1207:1717; I. Low, J. Lykken, and G. Shaughnessy, arXiv:1207:1344 [hep-ph]; S. Banerjee, S. Mukhopadhyay, and B. Mukhopadhyay, arXiv:1207:3588 [hep-ph]; F. Bonetti *et al.*, arXiv:1207:4599 [hep-ph]; T. Plehn and M. Rauch, arXiv:1207.6108 [hep-ph].
 - [7] B. Colleppa, K. Kumar and H.E. Logan, arXiv:12082692[hep-ph]; see also plenary talk by D. Zeppenfeld, SUSY 2012, Beijing, August 13–19 2012.
 - [8] J. R. Dellaquila and C. A. Nelson, Phys. Rev. D **33**, 80 (1986).
 - [9] C. A. Nelson, Phys. Rev. D **37**, 1220 (1988).
 - [10] A. Soni and R. M. Xu, Phys. Rev. D **48**, 5259 (1993).
 - [11] V. Barger *et al.*, Phys. Rev. D **49**, 79 (1994).
 - [12] B. C. Allanach *et al.*, JHEP **0212**, 039 (2002).
 - [13] S. Y. Choi, D. J. Miller, M. M. Muhlleitner, and P. M. Zerwas, Phys. Lett. B **553**, 61 (2003).
 - [14] C. P. Buszello, I. Fleck, P. Marquard, and J. J. van der Bij, Eur. Phys. J. C **32**, 209 (2004).
 - [15] R. M. Godbole, D. J. Miller, and M. M. Muhlleitner, J. High Energy Phys. **12**, 031 (2007).
 - [16] W. Y. Keung, I. Low, and J. Shu, Phys. Rev. Lett. **101**, 091802 (2008).
 - [17] O. Antipin and A. Soni, J. High Energy Phys. **10**, 018 (2008).
 - [18] K. Hagiwara, Q. Li, and K. Mawatari, J. High Energy Phys. **07**, 101(2009).
 - [19] Y.Y. Gao *et al.*, Phys. Rev. D **81**, 075022 (2010).

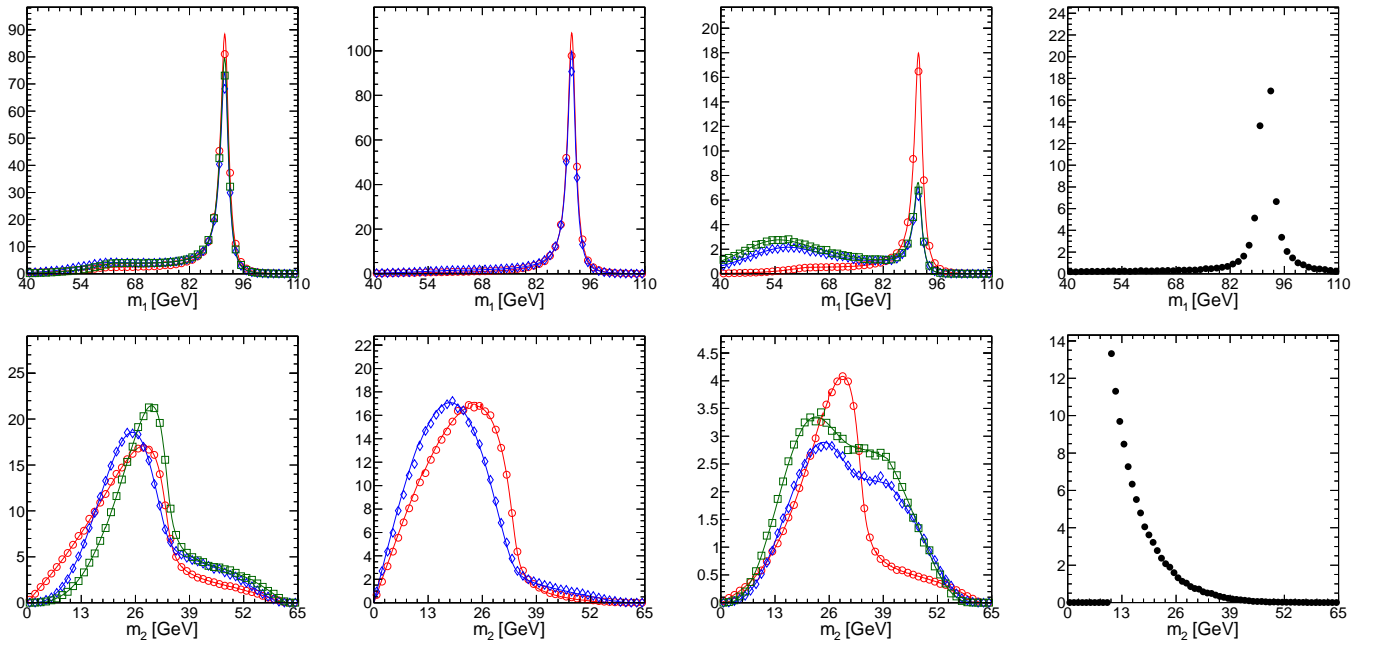


FIG. 11: Distributions of the observables in the $X \rightarrow ZZ$ analysis, from left to right: spin-zero, spin-one, and spin-two signal, and $q\bar{q} \rightarrow ZZ$ background. The signal hypotheses shown are J_m^+ (red circles), J_h^+ (green squares), J_h^- (blue diamonds), as defined in Table I. Background is shown with the requirements $m_2 > 10$ GeV and $120 < m_{4\ell} < 130$ GeV. The observables shown from top to bottom: m_1 and m_2 (where $m_1 > m_2$). Points show simulated events and lines show projections of analytical distributions.

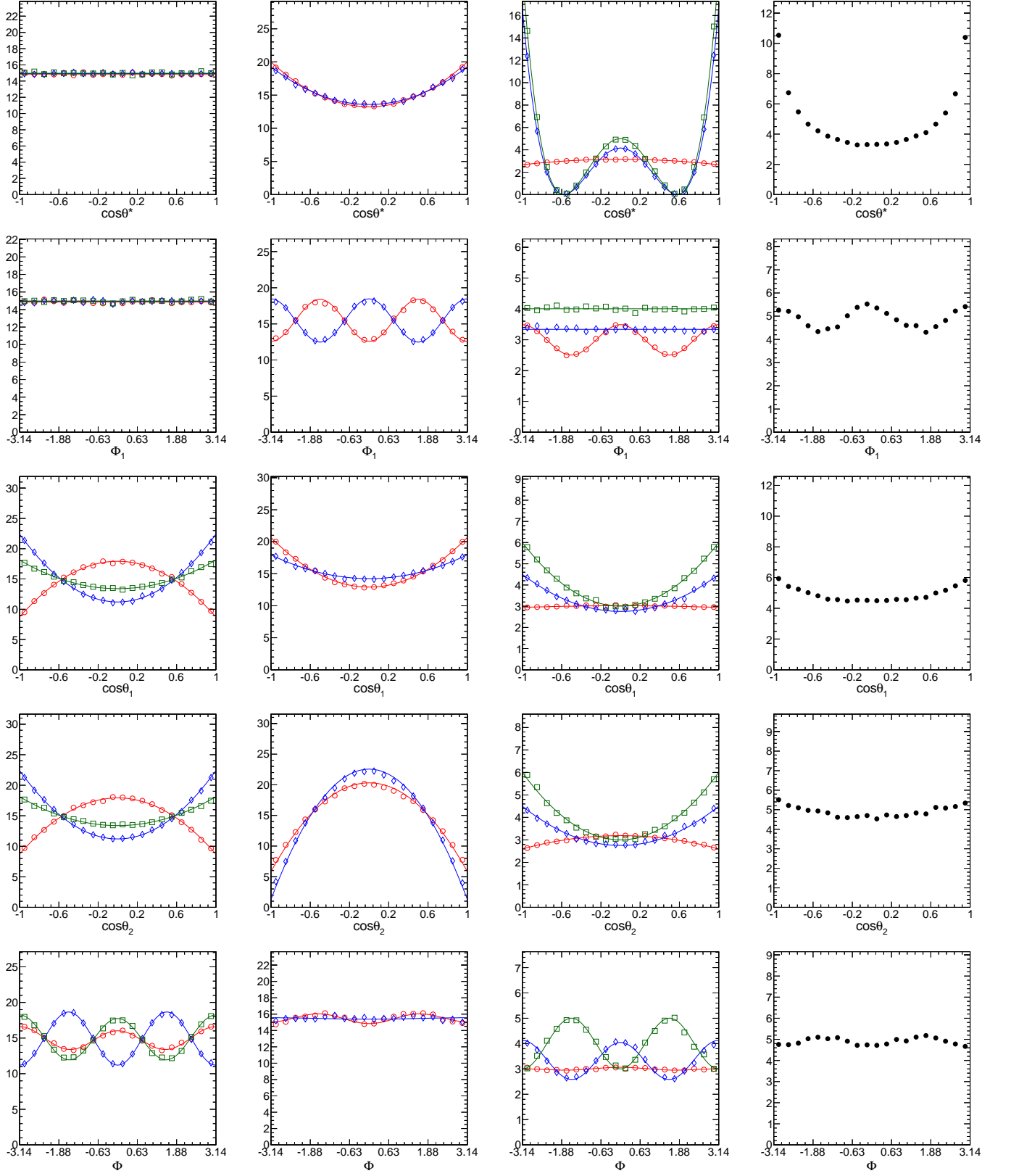


FIG. 12: Distributions of the observables in the $X \rightarrow ZZ$ analysis, from left to right: spin-zero, spin-one, and spin-two signal, and $q\bar{q} \rightarrow ZZ$ background. The signal hypotheses shown are J_m^+ (red circles), J_h^+ (green squares), J_h^- (blue diamonds), as defined in Table I. Background is shown with the requirements $m_2 > 10$ GeV and $110 < m_{A\ell} < 140$ GeV. The observables shown from top to bottom: $\cos\theta^*$, Φ_1 , $\cos\theta_1$, $\cos\theta_2$, and Φ . Points show simulated events and lines show projections of analytical distributions.

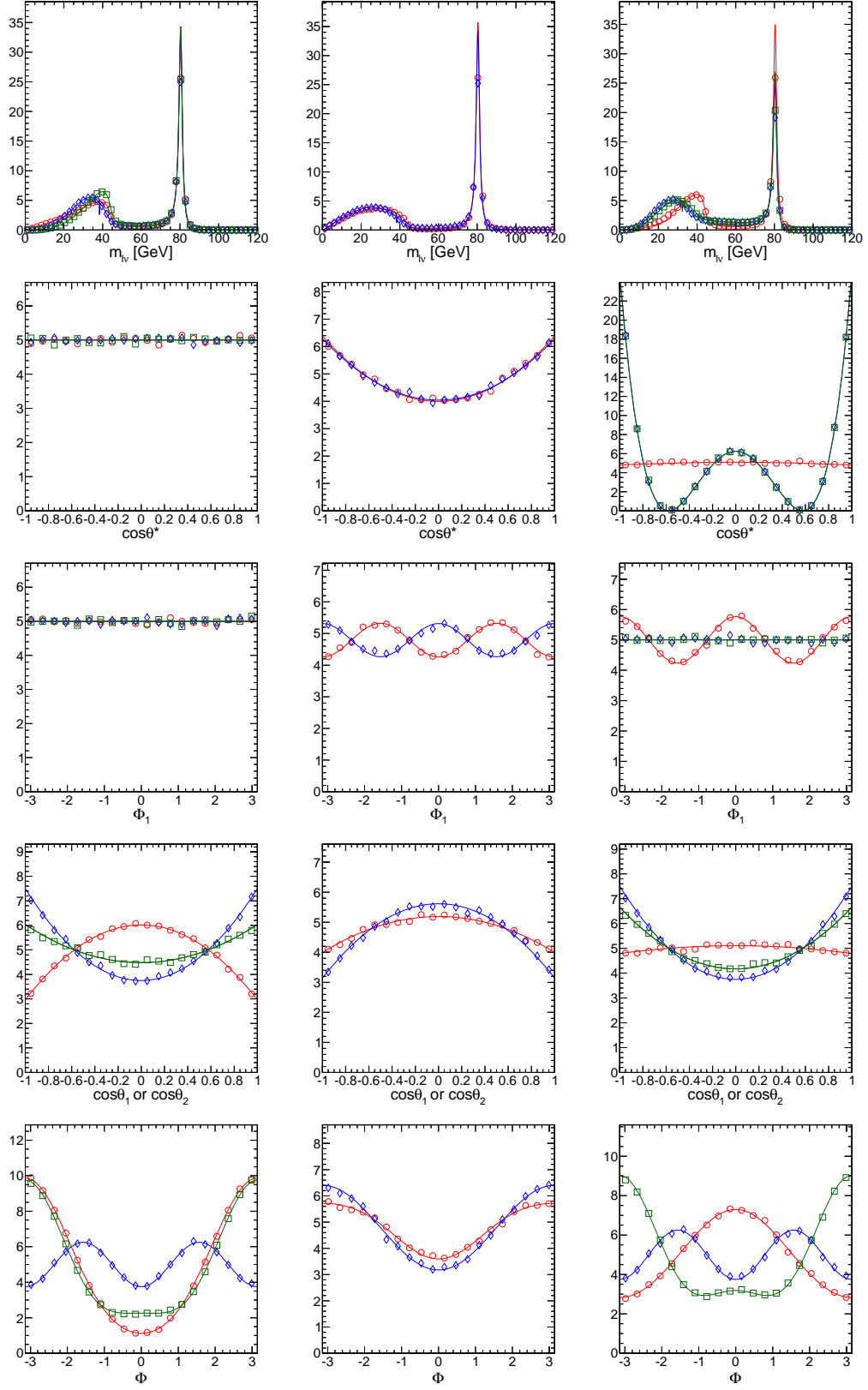


FIG. 13: Distributions of the observables in the $X \rightarrow WW$ analysis, from left to right: spin-zero, spin-one, and spin-two signal. The signal hypotheses shown are J_m^+ (red circles), J_h^+ (green squares), J_h^- (blue diamonds), as defined in Table I. The observables shown from top to bottom: $m_{1,2}$, $\cos\theta^*$, Φ_1 , $\cos\theta_{1,2}$, and Φ . Points show simulated events and lines show projections of analytical distributions.

- [20] A. De Rujula *et al.*, Phys. Rev. D **82**, 013003 (2010).
- [21] J. S. Gainer *et al.*, HEP **1111**, 027 (2011).
- [22] J. Ellis and D. S. Hwang, to appear in JHEP, arXiv:1202.6660 [hep-ph].
- [23] CMS collaboration, JHEP **04**, 036 (2012).
- [24] R. H. Dalitz, Proc. Phys. Soc. London Sect. A **64**, 667 (1951).
- [25] M. Jacob and G. C. Wick, Ann. Phys. **7**, 404 (1959).
- [26] N. Cabibbo and A. Maksymowicz, Phys. Rev. **137**, 438 (1965).
- [27] I. Dunietz *et al.*, Phys. Rev. D **43**, 2193 (1991).
- [28] G. Kramer and W. F. Palmer, Phys. Rev. D **45**, 193 (1992).
- [29] Particle Data Group, Phys. Rev. D **86**, 010001 (2012).
- [30] A. V. Gritsan and J. G. Smith, see review "Polarization in B decays" in Ref. [29].
- [31] J. C. Collins and D. E. Soper, Phys. Rev. D **16**, 2219 (1977).
- [32] J. F. Gunion, Y. Jiang and S. Kraml, arXiv:1207.1545 [hep-ph].
- [33] The Monte-Carlo generator, the manual, and supporting material can be downloaded from <http://www.pha.jhu.edu/spin/>
- [34] T. Sjostrand, S. Mrenna, and P. Skands, JHEP **05**, 026 (2006).
- [35] P. Nason, JHEP **11**, 040 (2004); S. Frixione, P. Nason, and C. Oleari, JHEP **11**, 070 (2007); S. Alioli *et al.*, JHEP **07**, 060 (2008).
- [36] J. Alwall *et al.*, JHEP **0709**, 028 (2007).
- [37] J. Pumplin *et al.*, JHEP **0207**, 012 (2002); P. M. Nadolsky *et al.*, Phys. Rev. D **78**, 013004 (2008).
- [38] Signal hypothesis separation discussion and kinematic distributions in the ZZ channel are not included in Ref. [2], for more details see J. Incandela, for CMS collaboration, CERN seminar, July 4, 2012; A. V. Gritsan, for CMS collaboration, FNAL seminar, July 9, 2012.
- [39] CMS collaboration, Phys. Rev. D **84**, 112002 (2011).